Material Matters™

Volume 6, Number 4

ALDRICH Materials Science

Materials for Energy Efficiency

Thermoelectrics, Thin Films, and Phosphors

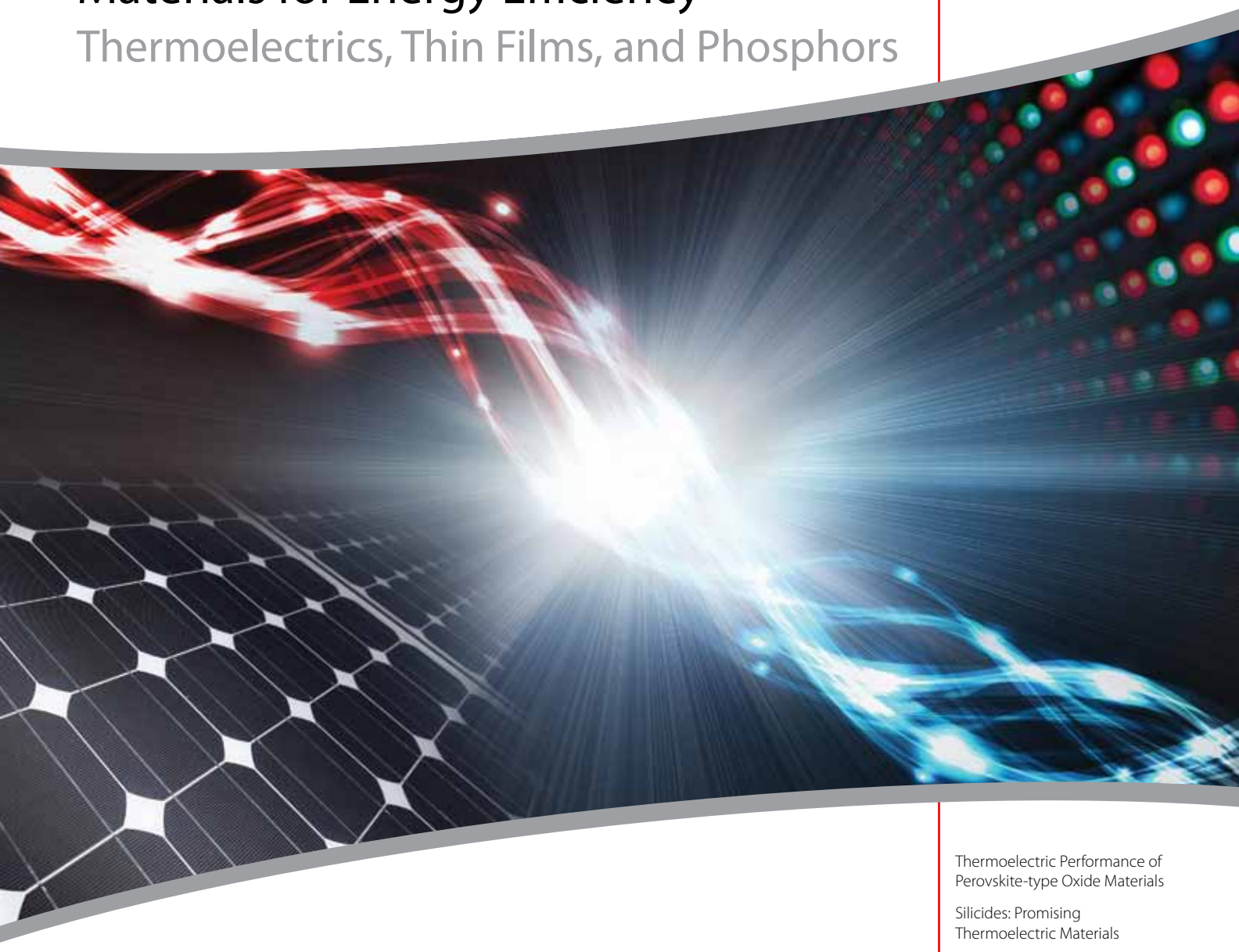

Hot Research, Cool Results

Introduction

Meenakshi Hardi, Ph.D.
Aldrich Materials Science
Sigma-Aldrich Co. LLC

Welcome to the fourth issue of ***Material Matters™*** for 2011, focusing on *Materials for Energy Efficiency: Thermoelectrics, Thin Films and Phosphors.*

Global energy demands are continuing to increase. To date, fossil fuels have served as a major energy source, to meet these ever growing energy needs. It is generally accepted that while fossil fuel technology is well developed, it is not sustainable and its subsequent carbon footprint is the contributing factor to global warming. Climate change, increasing energy demands and depletion of conventional energy sources all indicate that alternative energy must play a bigger role in the future. Alternative energy sources are renewable, and environmentally clean. These include solar power, hydrogen energy, and biofuel as well as wind, hydroelectric and geothermal energy.

In addition to developing alternative energy sources to meet growing energy requirements, it is equally important to improve the efficiency of energy generation. Energy efficiency and alternative energy are said to be the "twin pillars" of sustainable energy policy. Approximately 90% of the world's electricity is generated by thermal energy, typically operating at only 30–40% efficiency, losing a major portion of the energy in the form of radiant heat to the environment. Materials exhibiting the thermoelectric effect, a phenomenon in which a temperature difference creates an electric potential or vice versa, can convert some of this lost heat into useful electricity, thus increasing the overall efficiency of the energy generation. Thermoelectric materials have also been explored for other applications, for example, to capture heat lost in the exhaust of automobiles to produce electricity for the vehicle.

An alternative way of generating electricity is by using solar cells, which converts the energy of light into electricity by photovoltaic effect. Solar energy is one of the most promising sustainable energy sources. Solar currently contributes less than 1% of the world's energy supply. The relatively high cost per kilowatt-hour and the efficiency of commercial solar cells have limited their utility. The main loss of efficiency in the conversion of solar energy into electrical energy is due to spectral mismatch, wherein the low energy photons are not absorbed and high energy photons are not efficiently used by a solar cell. Spectral conversion by using materials, such as lanthanides with high luminescence efficiencies and rich energy level structure, can covert these high and low energy photons to desired wavelengths, thus significantly increasing the efficiency of solar cells.

The focus of this issue of ***Material Matters™*** is Materials for Energy Efficiency. The first two articles highlight novel thermoelectric materials, which are not based on widely used chalcogenides. In the first article, Prof. Anke Weidenkaff (EMPA-Swiss Federal Laboratories for Materials Science and Technology, Switzerland) describes the advantages of perovskite-type oxide materials, such as their flexibility and relatively simple and predictable structure–property relationship, thus making them novel thermoelectric materials. In the second article, Prof. Mikhail Fedorov (Ioffe Physical-technical Institute, St. Petersburg, Russia) describes metal silicides as another class of promising thermoelectrics. Prof. Bruce van Dover from Cornell University, USA, reports an efficient way of screening materials for different energy-related applications using the Codeposited Composition Spread (CCS) technique—a variant of high-throughput synthesis methods. In the last article, Prof. Andries Meijerink from Utrecht University, Netherlands, explores the emerging concept of spectral conversion in the field of photovoltaics, by using lanthanide ions to increase the efficiency of solar cells.

Each article in this publication is accompanied by a list of relevant materials available from Aldrich Materials Science. For additional product information, please visit Aldrich Materials Science at **Aldrich.com/matsci**. Please send us your comments or suggestions for ***Material Matters™*** or your product suggestions at **matsci@sial.com**.

About Our Cover

The development of advanced materials and technologies with improved performances for producing and storing energy is essential for securing our energy future. Examples of materials for energy efficiency include thermoelectric materials (p. 92 and p. 100), advanced thin films (p. 106) and luminescent materials (p. 113). The cover art of this issue represents the generation of energy through these energy efficient approaches, as illustrated through the hot and cold wave (thermal gradient for thermoelectrics) and phosphor materials for enhancing solar cells.

Material Matters™
Vol. 6, No. 4

Aldrich Materials Science
Sigma-Aldrich Co. LLC
6000 N. Teutonia Ave.
Milwaukee, WI 53209, USA

To Place Orders

Telephone	800-325-3010 (USA)
FAX	800-325-5052 (USA)

Customer & Technical Services

Customer Inquiries	800-325-3010
Technical Service	800-231-8327
SAFC®	800-244-1173
Custom Synthesis	800-244-1173
Flavors & Fragrances	800-227-4563
International	414-438-3850
24-Hour Emergency	414-438-3850
Website	**sigma-aldrich.com**
Email	aldrich@sial.com

Subscriptions

To request your **FREE** subscription to *Material Matters*, please contact us by:

Phone:	800-325-3010 (USA)
Mail:	Attn: Marketing Communications Aldrich Chemical Co., Inc. Sigma-Aldrich Co. LLC P.O. Box 2988 Milwaukee, WI 53201-2988
Website:	**Aldrich.com/mm**
Email:	sams-usa@sial.com

International customers, please contact your local Sigma-Aldrich office. For worldwide contact information, please see back cover.

Material Matters is also available at **Aldrich.com/matsci**.

Material Matters (ISSN 1933–9631) is a publication of Aldrich Chemical Co., Inc. Aldrich is a member of the Sigma-Aldrich Group.

Your Materials Matter.

Jeff Thurston, President
Aldrich Chemical Co., Inc.

Do you have a compound that you wish Aldrich® Materials Science could list to help materials research? If it is needed to accelerate your research, it matters—send your suggestion to ***matsci@sial.com*** *and we will be happy to give it careful consideration.*

Dr. Jacques Huot of Université du Québec à Trois-Rivières kindly suggested that we offer high purity magnesium ingots (Aldrich Prod. No. 735779), suitable for the preparation of hydrogen storage metals. Recent studies have shown that cold-processing of bulk magnesium can drastically increase hydrogen sorption properties relative to untreated powdered magnesium.[1] Magnesium is also used in the production of biodegradable implants (Mg-Mn-Zn),[2] battery materials,[3] light weight structural alloys (Mg-Al and Mg-Al-Zn),[4-5] and corrosion resistance coatings for steel parts.[6-7]

Larger forms of elemental magnesium can be used in metallurgical processes and are beneficial due to a reduced amount of surface oxidation compared to magnesium powder or turnings.

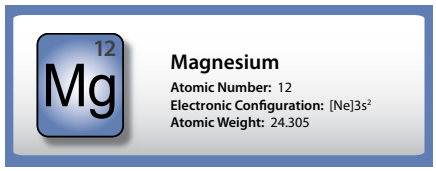

Magnesium, ≥99% trace metals basis

[7439-95-4] BRN 4948473 Mg FW 24.31

resistivity ..... 4.46 µΩ-cm, 20 °C
mp ..... 648 °C vp ..... 1 mmHg (621 °C)
bp ..... 1090 °C ait ..... 950 °F
density ..... 1.74 g/mL, 25 °C

▸ **ingot**
L × W × H ..... 100 mm × 100 mm × 50 mm

735779-1EA 1 ea

References

1. Huot, J.; Balema, V. *Material Matters* **2010**, *5*, 112.
2. Xu, L.; Pan, F.; Yu, G.; Yang, L.; Zhang, E.; Yang, K. *Biomaterials* **2009**, *30*, 1512.
3. Pedneault, S.; Huot, J.; Roue, L. *J. Power Sources* **2008**, *185*, 566.
4. Pardo, A.; Merino, M.C.; Coy, A.E.; Arrabal, R.; Viejo, F.; Matykina, E. *Corros. Sci.* **2008**, *50*, 823.
5. Huang, X.; Suzuki, K.; Watazu, A.; Shigematsu, I.; Saito, N. *J. Alloys Compd.* **2008**, *457*, 408.
6. Ambat, R.; Aung, N.N.; Zhou, W. *Corros. Sci.* **2000**, *42*, 1433.
7. Jiang, Z.; Li, S.; Zeng, J.; Liao, X.; Yang, D. *Adv. Mater. Res.* **2011**, *189-193*, 1248.

Table of Contents

Articles

Featured Products

Thermoelectric Performance of Perovskite-type Oxide Materials



Lassi Karvonen, Petr Tomeš, Anke Weidenkaff*
Laboratory for Solid State Chemistry and Catalysis
Department of Mobility, Energy and Environment
EMPA-Swiss Federal Laboratories for Materials Science and Technology
Überlandstrasse 129, CH-8600 Dübendorf, Switzerland
*Email: anke.weidenkaff@empa.ch

Global Energy Challenge

The prevailing strategies for heat and electric-power production that rely on fossil and fission fuels are having a negative impact on the environment and on our living conditions. Meanwhile, the global energy trend appears to show only an increasing demand for energy. Alternative and environmentally benign sources of primary energy do exist. However, development is ongoing for strategies to convey these alternative sources into desired energy forms that are adequately competitive with conventional technologies. In addition to alternative sources, improvement in the efficiency of energy-conversion is considered to be a part of the solution. For example, in the mechanical conversion of heat to electricity, a major part of the primary energy is lost to the environment. Therefore, technologies for harnessing the dissipating heat component are highly desired. Direct thermoelectric power conversion, omitting any mechanical intermediate stage, is seen as one of the more promising strategies.

Thermoelectric Power Conversion

A thermoelectric generator (**Figure 1**) consists of an alternating series of *n*- and *p*-type conducting legs that are connected in series to the applied electric field and parallel to the heat gradient applied over the generator module. The Seebeck effect, caused by the heat gradient, accumulates the majority of the charge carriers on the cold side of each leg, thereby building up a net voltage across the electrically coupled series.

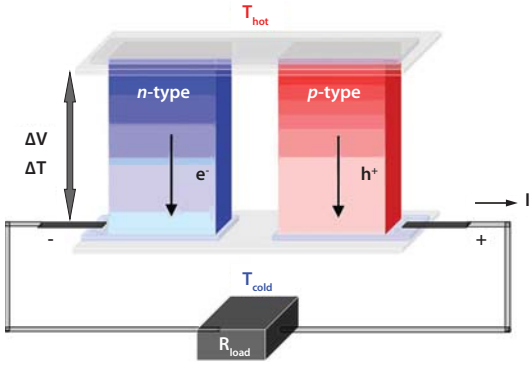

Figure 1. A schematic diagram of a thermoelectric generator, consisting of *n*- and *p*-type legs coupled electrically in series and thermally in parallel.

A good thermoelectric leg material combines a high thermopower (Seebeck coefficient, *S*) with a low thermal conductivity (κ) and low electrical resistivity (ρ). This is often expressed in terms of maximizing the dimensionless figure of merit $ZT = S^2T/\rho\kappa$, which is directly related to maximizing the efficiency of the heat-to-electricity conversion and approaching the Carnot limit at $ZT \rightarrow \infty$.[1]

Since all the considered quantities deal with the charge-carrier mobility and density or the density of electronic states, achieving simultaneous improvements in all of them is challenging. As a compromise of the properties, the best-known and currently most widely applied thermoelectric materials are found among the semiconducting materials, particularly chalcogenides such as Bi_2Te_3 (Aldrich Prod. No. 751421), $Bi_{2-x}Sb_xTe_3$ (Aldrich Prod. No. 752509), and $Bi_2Te_{3-x}Se_x$.[2] The chalcogenide materials already reaching the application stage present *ZT* values of ~1 and are also currently considered a limit for commercial interest. While the highest *ZT* values for any bulk thermoelectric material to date are around 1.5, reaching the efficiencies of the compressor-run heat engines still demands at least double that value.[3] However, since the wasted heat generally does not have alternative uses, even the modules with $ZT < 1$ materials could be considered as beneficial supplements to available energy conversion technologies.

Oxides as Thermoelectric Materials

The poor chemical and physical stability under high temperatures of chalcogenides, as well as oxidizing conditions, along with relatively high toxicity, make them incompatible with major energy conversion technologies operating in air ambient conditions, e.g., combustion engines, concentrated solar radiation sources, or furnaces.[4-6] Oxide materials, on the other hand, are very durable under these conditions. Although generally considered as insulators with a high Seebeck coefficient, some oxide materials are able to present *ZT* values that are comparable to semiconducting chalcogenides (**Figure 2**). Currently, the best performing oxide materials present rather low $ZT \sim 0.3$ in polycrystalline form.[7,8] However, a better understanding of the effects of the synthesis parameters on the microstructure and on the physical properties of the materials is expected to deliver a great improvement. As an example, experiments with Na_xCoO_2 and $[Ca_2CoO_3]_{0.62}[CoO_2]$ layered-cobalt-oxide single crystals have indicated that *ZT* can be enhanced up to and beyond 1.[9,10] Oxide compounds, currently considered to have the most potential of all thermoelectric materials, can be divided into three main groups: layered complex oxides, doped zinc oxide derivatives, and perovskite-type oxides.

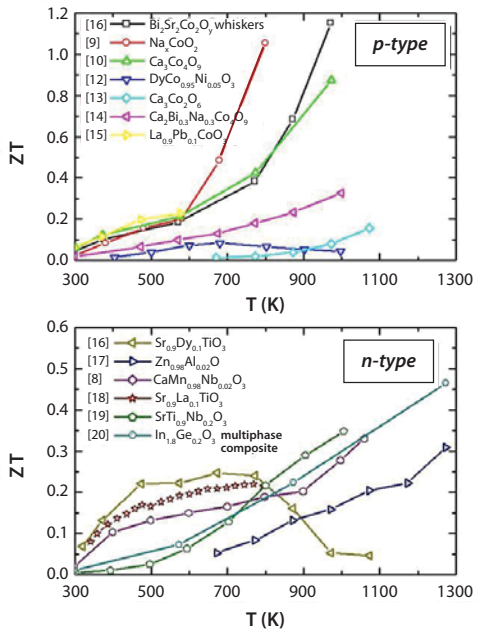

Figure 2. Figure of Merit (*ZT*) of selected oxide materials.

As mentioned above, the layered complex oxides, such as $Na_{0.50}CoO_2$[21] and the extended family of misfit-layered oxides $[M_mA_2O_{m+2}]^{RS}_q[CoO_2]^H$ (*M* = Co, Bi, Pb, Tl, etc.; *A* = Ca, Sr, Ba, etc.; *m* = 0, 1, 2; *q* ≥ 0.5),[22] have presented the highest *ZT* values for the oxides. In addition to being relatively good electrical conductors, the main reason for their performances are their high Seebeck coefficients (80 μV K^{-1} < *S* < 170 μV K^{-1}) when compared to the conductivity due to a large spin- and orbital entropy of the tetravalent low-spin cobalt (Co^{4+}) in the $[CoO_2]$ layer block.[23]

Zinc oxide (Aldrich Prod. No. 204951), also known as a transparent conducting oxide (TCO) material, has received notable attention as a potential thermoelectric material. For example, $Zn_{0.98}Al_{0.02}O$ thin films have shown a reasonably high *ZT* ~ 0.3 at *T* = 1273 K.[24] This is mainly due to enhancement of the electrical conductivity, which is more than three orders of magnitude higher than the value of the unsubstituted material. *ZT* also benefits the Seebeck coefficient by staying at rather elevated values, such as *S* > 100 μV K^{-1} at 300 K < *T* < 1273 K, despite the charge-carrier doping through aluminum substitution.

The major advantages of the perovskites are their profound flexibility in terms of the constituent elements covering most of the periodic table, which provides a broad selection of material-property combinations to explore. While simple perovskite-type compounds with high Seebeck coefficients are normally good insulators and, as such, not very strong potential thermoelectric materials, fruitful compromises between the lowered *S* and ρ are achievable through aliovalent cation substitutions. The S^2/ρ factor inside the *ZT* equation, commonly known as the *power factor*, is maximized by introducing charge carriers.[25-27]

Thermoelectric Engineering of the Perovskite Oxide Materials

The electron-band structure of the cubic perovskite close to the Fermi level (E_f) typically consists of transition metal (*TM*) *d*-orbitals mixing with O2*p* orbitals. Octahedral *TM*-O coordination splits the *TM*-*d* orbitals into two subsets: the triply degenerate t_{2g} orbitals and the doubly degenerate e_g orbitals. The landing of the E_f at either of these orbital sets depends on the *d*-electron population affected by the *TM* valence and the *TM*-O charge-transfer condition.[28] Among the given candidates for the thermoelectric perovskite-oxide materials, the Fermi level resides across the t_{2g} orbitals. Consequently, the relatively high degree of spin-degeneration has an improving effect on the effective mass of a single charge carrier[29] leading to the detected high Seebeck values through an elevated charge carrier entropy. The aim of the substitutions is to lower the electrical resistivity by presenting additional charge carriers at E_f, while simultaneously conserving the feasible *d*-orbital degeneracy. Therefore, *n*-type materials are doped with electrons typically through substituting lower-valent cations of the conductive *TM*-O network with higher-valent ones. Conversely, for the *p*-type cobaltates, higher valent cations need to be substituted with lower-valent ones. Ideally, an appropriate substituent should not present major changes to the crystal-structure that would undermine either the orbital degeneracy through distortions of the octahedral *TM*-O coordination environment or the *TM*d-O2*p* orbital overlap through lattice distortions or expansions.[19]

Of the substituted perovskite compounds, substituted titanates $Sr_{1-x}A_xTi_{1-y}Nb_yO_3$ (*A* = Ca, La, Ba, Eu),[19] manganates $CaMn_{1-x}Nb_xO_3$,[8] and rare-earth cobaltates $LnCo_{1-x}Ni_xO_3$ (*Ln* = La, Pr, Nd, Sm, Gd, Dy) present the most promising *ZT* values.[12] The *n*-type conducting $SrTiO_3$ is especially known for its structural flexibility over a wide range of substitutions. The record-high *ZT* ~ 0.37 at *T* = 1000 K among perovskite oxides is measured for the $SrTi_{0.8}Nb_{0.2}O_3$ thin films,[30] while *ZT* ~ 0.35 at *T* = 1073 K has been achieved for a hot-pressed bulk sample of the same composition.[7] However, as titanium prefers to exist in its group valence state as Ti^{4+}, the Nb^{5+}-substitution-induced Ti^{3+} tends to re-oxidize at *T* > 600 K, rejecting the air-operating high-temperature applications.[19] Manganates, also *n*-type conducting, present several stable oxidation states that make them useful when considering oxidizing atmospheres.[19] The record *ZT* ~ 0.32 at *T* = 1060 K for the manganates was reached with the polycrystalline $CaMn_{0.98}Nb_{0.02}O_3$.[8] The formation of twinned structures of orthorhombically distorted domains at low-temperatures is characteristic for the $CaMnO_3$-based systems, while a cubic symmetry, which improves the thermoelectric properties, is realized at a high temperature range.[27] Lanthanide cobaltates present the *p*-type conductive materials among the thermoelectric perovskites. They are well-known for their thermally activated spin-state transitions, which can be affected by the *Ln* substituent. The maximum *ZT* values for all of them are rather similar, ranging from 0.07-0.08. However, a smaller radius of the substituent cation pushes the low-temperature, low-spin to intermediate-spin and pushes the high-temperature, intermediate-spin to high-spin transitions and towards even higher temperatures, which affects the temperature of the *ZT* maximum. Depending on the applied temperature range, the $LnCoO_3$ with appropriate *ZT* may then be chosen.

The highest *ZT* values, ranging between 0.3 and 0.4, are reached normally at low substitution levels (x, y < 0.2). As an extreme example, only $x = 0.02$ is necessary in order to reach the maximum *ZT* for the $CaMn_{1-x}Nb_xO_3$ system, beyond which the *ZT* value begins to decrease. Such a low substitution level sets requirements concerning the homogeneity of the unsintered solid-state precursor material, as spatial fluctuations with the chemical composition across the sintered body easily lead to unpredictability and instability of the properties of the sintered bodies from one synthesis batch to another. In such cases, soft-chemical procedures are favored, where initial mixing of the constituent cations takes place in solutions of strong organic chelating agents (e.g., EDTA, citric acid) conserving the homogeneous cation mixture over the subsequent drying, charring, and calcinations steps (**Figure 3**) down to the atomic scale.[8]

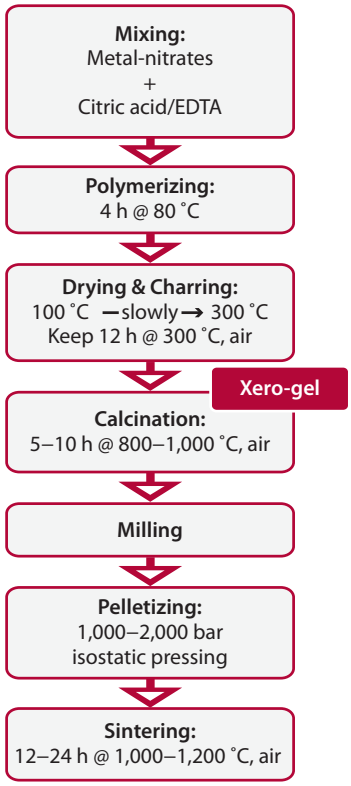

Figure 3. Flow-sheet describing a typical soft-chemical synthesis procedure for producing oxide thermoelectric materials.

While the power factor can be significantly improved through substitutions, the persistent high value of κ has hindered the *ZT* from reaching values much above 0.3. Substitution by heavier cations has an observable effect, but the structural distortions reducing the electronic performance tend to outweigh the benefits. In terms of thermal-conductivity suppression, the shortcomings with the perovskite lattice arise from its relatively high structural isotropicity. As compared to a typical phononic mean free path length of a few hundreds of angstroms, simple perovskites are described by translational periodicities of a few angstroms. In order to improve phononic scattering, intrinsic longer-range discontinuities, interfaces, and grain boundaries with intervals approaching the phonon, mean-free path lengths should thus be introduced. Much work on the nanostructurization has been done lately,[19] and several ideas, such as using layered perovskite derivatives and artificial layered superlattice structures, are currently under development or being implemented. Additionally, a nanostructurization approach aiming at a network of charge-carrier doped interfaces in an insulating matrix that presents thicknesses of only a few unit cells is expected to provide a massive improvement to the Seebeck coefficient through increased density of states at E_f due to quantum confinement. A recent highlight that proves the concept is the observation of $ZT \sim 2.4$ at 300 K in an artificially grown superlattice, where a single layer of $SrTi_{0.8}Nb_{0.2}O_3$ is sandwiched between several layers insulating $SrTiO_3$. A shortcoming of the approach is that the insulating matrix accounts for most of the material, thereby returning the *ZT* of the entire superlattice back below 0.3.[31]

Combining *n*- and *p*-Type Oxide Materials into a Thermoelectric Generator

Good thermoelectric conversion efficiencies require leg materials with similar physical properties. The thermoelectric compatibility factor, $s = |(1+ZT)^{0.5}-1|/(ST)$, describes the reduced electric current necessary for achieving the highest efficiency determined by *ZT* of the material.[32] For maximum conversion efficiency of the thermoelectric generator, the *s* values of the *n*- and *p*-type materials to be combined should be as similar as possible within the operating temperature range and their ratio generally < 2. The significance of the compatibility is demonstrated as follows:

$CaMn_{0.98}Nb_{0.02}O_3$ (*n*-type)/$GdCo_{0.95}Ni_{0.05}O_3$ (*p*-type)

Thermoelectric properties of $CaMn_{0.98}Nb_{0.02}O_3$ and $GdCo_{0.95}Ni_{0.05}O_3$ materials are given in **Figure 4**.

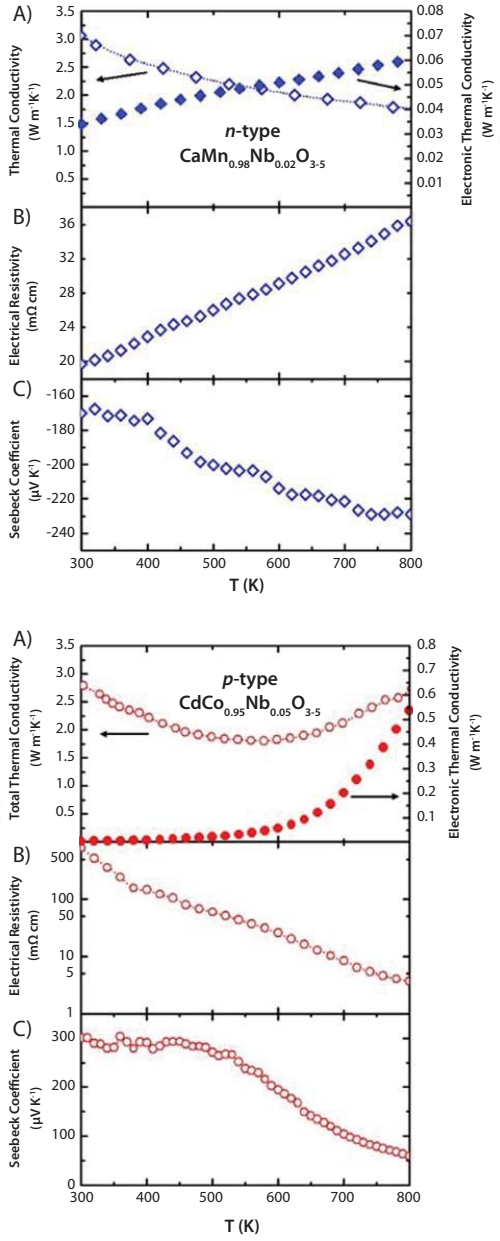

Figure 4. Temperature dependence of the thermoelectric properties A) κ, B) ρ and C) S of *n*-type $CaMn_{0.98}Nb_{0.02}O_3$ (top panel) and *p*-type $GdCo_{0.95}Ni_{0.05}O_3$ (bottom panel).

The $\kappa = \kappa_{ph} + \kappa_{el}$ of both materials (**Figure 4A**) are close to 3 $Wm^{-1}K^{-1}$ above 300 K. The thermal conductivity of the $GdCo_{0.95}Ni_{0.05}O_3$ leg (**Figure 4A**, bottom) increases by 50 % and is between 600 K and 800 K; this is attributed to an increase in the electronic part (κ_{el}) due to a spin-state transition increasing the charge carrier mobility - fairly typical for the $LnCoO_3$-based systems. On the other hand, the $CaMn_{0.98}Nb_{0.02}O_3$ leg (**Figure 4A**, top) shows a monotonic decrease in thermal conductivity over the observed temperature scale, which is understood to arise dominantly from the phononic part of the thermal conductivity (κ_{ph}).

The resistivity of $CaMn_{0.98}Nb_{0.02}O_3$ (**Figure 4B**, top) indicates metal-like temperature behavior ($d\rho/dT > 0$) with a steady decrease of the Seebeck coefficient, whereas semiconducting-like behavior ($d\rho/dT < 0$) with relevantly higher resistivity is observed for $GdCo_{0.95}Ni_{0.05}O_3$ (**Figure 4B**, bottom). The slope of the $GdCo_{0.95}Ni_{0.05}O_3$ Seebeck coefficient features a down-turn also related to the spin-state transition, as described above (**Figure 4C**, bottom). Both materials show similar ZT values at a range of $T < 600$ K. However, at $T > 600$ K, the slope of the $GdCo_{0.95}Ni_{0.05}O_3$ turns negative because the more negative slope of the Seebeck coefficient degrades the performance of the generator at $T > 600$ K. Furthermore, the high electrical resistivity of $GdCo_{0.95}Ni_{0.05}O_3$ at $T < 600$ K keeps the total internal resistance of the module high and also within a low-temperature range.

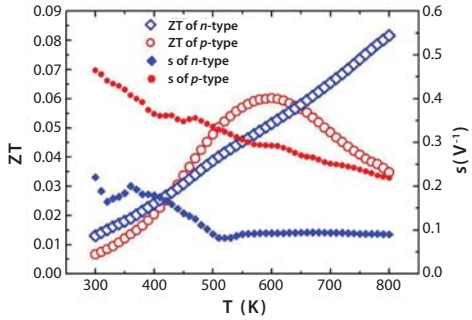

Figure 5. Figure of Merit (ZT) and thermoelectric compatibility factor (s) of the *p*-type $GdCo_{0.95}Ni_{0.05}O_3$ and the *n*-type $CaMn_{0.98}Nb_{0.02}O_3$ materials.

The thermoelectric compatibility factors of $CaMn_{0.98}Nb_{0.02}O_3$ and $GdCo_{0.95}Ni_{0.05}O_3$ are presented in **Figure 5**. Difference by s factor of 2-4 indicates a notably low expectable output. To overcome the difference in compatibility factors, an alternative *p*-type material, $La_{1.98}Sr_{0.02}CuO_4$, was tested instead of the $GdCo_{0.95}Ni_{0.05}O_3$ material.

$$CaMn_{0.98}Nb_{0.02}O_3\ (n\text{-type})/La_{1.98}Sr_{0.02}CuO_4\ (p\text{-type})$$

The thermoelectric properties of the materials are summarized in **Figure 6**.

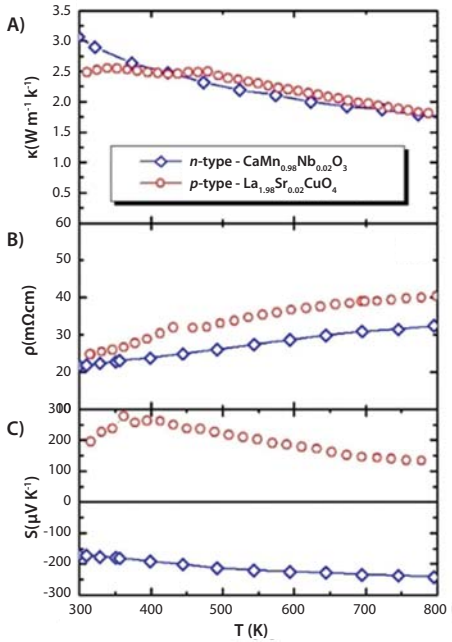

Figure 6. Temperature dependence of A) κ, B) ρ and C) S of the *p*-type $La_{1.98}Sr_{0.02}CuO_4$ and the *n*-type $CaMn_{0.98}Nb_{0.02}O_3$ materials.

The thermal conductivities (**Figure 6A**) and resistivities (**Figure 6B**) of both materials are similar in terms of magnitude and trend. Both appear to show metallic behavior and large Seebeck coefficients (**Figure 6C**).

The temperature dependence of the *ZT* (**Figure 7**) is sensitive to the Seebeck coefficient of $La_{1.98}Sr_{0.02}CuO_4$, which is manifested by the degradation of the *ZT* value above $T > 400$ K. The temperature dependence of the compatibility factors (**Figure 7**) indicates a closer similarity ($s < 2$) at a lower-temperature regime ($300\ K < T < 500\ K$). At $T > 500$ K, a decrease in the conversion efficiency of the four-leg modules was observed. Although the gross *ZT* characteristics of $La_{1.98}Sr_{0.02}CuO_4$, are poorer compared to the $GdCo_{0.95}Ni_{0.05}O_3$, a significant improvement due to a better compatibility delivered by similar electrical and thermal conductivities (**Figure 6C**) can be observed.

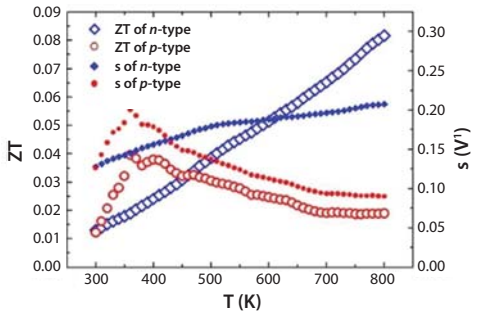

Figure 7. Temperature dependence of the Figure of Merit (*ZT*) and thermoelectric compatibility factor (*s*) of the *p*-type $La_{1.98}Sr_{0.02}CuO_4$ and the *n*-type $CaMn_{0.98}Nb_{0.02}O_3$ materials.

Summary

Thermoelectric heat-to-electricity conversion has received increasing attention over the past 15 years as one of the ways to improve the energy efficiency of the conventional electric-power production strategies. Thanks to their flexibility, perovskite-oxide materials and derivatives offer a wide range of possibilities to search and optimize novel thermoelectric materials. The advantages of the perovskites are their profound flexibility and relatively simple—and therefore predictable—structure-property relations. On the other hand, the simplicity of the perovskite structure can be seen as a challenge when considering the ways to suppress thermal conductivity. Despite lower performance compared to more conventional thermoelectric materials, such as chalcogenides, the all-oxide materials have their undisputable strengths, such as being able to operate at much higher temperatures and oxidizing atmospheres.

Acknowledgments

The Swiss Federal Office of Energy (SFOE), the Swiss National Science Foundation (SNF-MANEP), and Swisselectric are highly acknowledged for financial support. K. Koumoto, A. Maignan, and J. Hulliger are acknowledged for their fruitful discussions and scientific input. We also gratefully acknowledge the present and former members of the Solid State Chemistry and Catalysis lab at EMPA for their experimental results.

References

(1) *CRC Handbook of Thermoelectrics*; Rowe, D. M., Ed.; CRC Press: Boca Raton, 1995.
(2) Tritt, T. M. *Science* **1999**, *283*, 804.
(3) DiSalvo, F. J. *Science* **1999**, *285*, 703.
(4) Weidenkaff, A.; Robert, R.; Aguirre, M. H.; Bocher, L.; Lippert, T.; Canulescu, S. *Renewable Energy* **2008**, *33*, 342.
(5) Tomeš, P.; Robert, R.; Trottmann, M.; Bocher, L.; Aguirre, M. H.; Hejtmanek, J.; Weidenkaff, A. *J. Electr. Mater.* **2010**, *39*, 1696.
(6) Tomeš , P.; Suter , C.; Trottmann , M.; Steinfeld A.; Weidenkaff, A. *J. Mat. Res.* **2011**, *26*, 1975.
(7) Ohta, S.; Ohta, H.; Koumoto, K. *J. Ceram. Soc. Jpn.* **2006**, *114*, 102.
(8) Bocher, L.; Aguirre, M. H.; Logvinovich, D.; Shkabko, A.; Robert, R.; Trottmann, M.; Weidekaff, A. *Inorg. Chem.* **2008**, *47*, 8077.
(9) Fujita, K.; Mochida, T.; Nakamura, K. *Jpn. J. Appl. Phys.* **2001**, *40*, 4644.
(10) Shikano, M.; Funahashi, R. *Appl. Phys. Lett.* **2003**, *82*, 1851.
(11) Funahashi, R.; Shikano, M. *Appl. Phys. Lett.* **2002**, *81*, 1459.
(12) Robert, R.; Aguirre, M. H.; Hug, P.; Reller, A.; Weidenkaff, A. *Acta Mater.* **2007**, *55*, 4965.
(13) Mikami, M.; Funahashi, R.; Yoshimura, M.; Mori, Y.; Sasaki, T. *J. Appl. Phys.* **2003**, *94*, 5144.
(14) Xu, G.; Funahashi, R.; Shikano, M.; Matsubara, I.; Zhou, Y. *Appl. Phys. Lett.* **2002**, *80*, 3760.
(15) He, T.; Chen, J.; Calvarese, T. G.; Subramanian, M. A. *Solid State Sci.* **2006**, *8*, 467.
(16) Muta, H.; Kurosaki, K.; Yamanaka, S. *J. Alloys Compd.* **2003**, *350*, 292.
(17) Ohtaki, M.; Tsubota, T.; Eguchi, K.; Arai, H. *J. Appl. Phys.* **1996**, *79*, 1816.
(18) Liu, J.; Wang, C. L.; Su, W. B.; Wang, H. C.; Zheng, P.; Li, J. C.; Zhang, J. L.; Mei, L. M. *Appl. Phys. Lett.* **2009**, *95*, 162110.
(19) Koumoto, K.; Wang, Y.; Zhang, R.; Kosuga, A.; Funahashi, R. *Annu. Rev. Mater. Res.* **2010**, *40*, 363.
(20) Bérardan, D.; Guilmeau, E.; Maignan, A.; Raveau, B. *Solid State Commun.* **2008**, *146*, 97.
(21) Terasaki, I. *Phys. Rev. B.* **1997**, *56*, R12685.
(22) Yamauchi, H.; Karvonen, L.; Egashira, T.; Tanaka, Y.; Karppinen, M. *J. Solid State Chem.* **2011**, *184*, 64.
(23) Koshibae, W.; Tsutsui, K.; Maekawa, S. *Phys. Rev., B.* **2000**, *62*, 6869.
(24) Tsubota, T.; Ohtaki, M.; Eguchi, K.; Arai, H. *J. Mater. Chem.* **1997**, *7*, 85.
(25) Maignan, A.; Hebert, S.; Li, P.; Pelloquin, D.; Martin, C.; Michel, C.; Hervieu, M.; Raveau, B. *Crystal Engineering* **2002**, *5*, 365.
(26) Robert, R.; Bocher, L.; Sipos, B.; Döbeli, M.; Weidenkaff, A. *Prog. Solid State Chem.* **2007**, *35*, 447.
(27) Bocher, L.; Aguirre, M. H.; Robert, R.; Logvinovich, D.; Bakardjieva, S.; Hejtmanek, J.; Weidenkaff, A. *Acta Mater.* **2009**, *57*, 5667.
(28) Uchida K.; Tsuneyuki S.; Schimizu T. *Phys. Rev. B.* **2003**, *68*, 174107.
(29) Frederikse H. P. R.; Thurber W. R.; Hosler W. R. *Phys. Rev.* **1964**, *134*, A442.
(30) Ohta, S.; Nomura, T.; Ohta, H.; Hirano, M.; Hosono, H.; Koumoto, K. *Appl. Phys. Lett.* **2005**, *87*, 092108.
(31) Ohta H. *Mater. Today* **2007**, *10*, 44.
(32) Snyder, G. J. *Appl. Phys. Lett.* **2004**, *84*, 2436.

Materials for Perovskite Oxides

For a complete list of available materials, visit Aldrich.com/ceramics

Name	Composition	Purity	Form	Prod. No.
Calcium carbonate	$CaCO_3$	≥99.999% trace metals basis	powder	481807-5G 481807-25G
Calcium carbonate	$CaCO_3$	≥99.995% trace metals basis	powder and chunks	202932-5G 202932-25G 202932-100G
Calcium chloride hexahydrate	$CaCl_2 \cdot 6H_2O$	98%	solid	442909-1KG 442909-2.5KG
Calcium chloride	$CaCl_2$	≥99.99% trace metals basis	beads	429759-10G
Calcium hydroxide	$Ca(OH)_2$	99.995% trace metals basis	powder	450146-5G 450146-25G
Calcium isopropoxide	$Ca(OCH(CH_3)_2)_2$	≥99.9% trace metals basis	powder	497398-2G
Calcium methoxide	$Ca(OCH_3)_2$	97%	solid	445568-10G

Name	Composition	Purity	Form	Prod. No.
Calcium nitrate hydrate	$Ca(NO_3)_2{\cdot}xH_2O$	99.997% trace metals basis	crystals and lumps	202967-10G 202967-50G
Calcium oxide	CaO	99.995% trace metals basis	powder and chunks	229539-5G 229539-50G
Calcium oxide	CaO	99.9% trace metals basis	powder	208159-25G 208159-100G 208159-500G
Titanium(IV) butoxide	$Ti(OCH_2CH_2CH_2CH_3)_4$	≥97.0%, gravimetric	liquid	86910-250ML 86910-1L
Titanium(II) chloride	$TiCl_2$	99.98% trace metals basis	powder	451738-1G 451738-5G
Titanium(III) chloride	$TiCl_3$	≥99.995% trace metals basis	crystalline	514381-1G 514381-5G
Titanium(III) oxide	Ti_2O_3	99.9% trace metals basis	powder	481033-10G 481033-50G
Titanium(IV) butoxide	$Ti(OCH_2CH_2CH_2CH_3)_4$	97%	liquid	244112-5G 244112-100G 244112-500G 244112-2KG
Titanium(IV) ethoxide	$Ti(OC_2H_5)_4$	-	liquid	244759-50G 244759-250G
Titanium(IV) isopropoxide	$Ti[OCH(CH_3)_2]_4$	99.999% trace metals basis	liquid	377996-5ML 377996-25ML 377996-100ML
Titanium(IV) methoxide	$Ti(OCH_3)_4$	≥99.99% trace metals basis	powder	463582-25G
Titanium(IV) oxide, rutile	TiO_2	99.995% trace metals basis	powder and chunks	204730-5G 204730-25G
Titanium(IV) oxide, rutile	TiO_2	99.99% trace metals basis	powder	204757-25G 204757-125G
Titanium(IV) oxide, anatase	TiO_2	≥99% trace metals basis	powder	248576-100G 248576-1KG 248576-10KG
Titanium(IV) *tert*-butoxide	$Ti[OC(CH_3)_3]_4$	-	liquid	462551-25ML 462551-50ML
Manganese(II) carbonate	$MnCO_3$	≥99.9% trace metals basis	powder	377449-250G 377449-1KG
Manganese(II) chloride	$MnCl_2$	99.999% trace metals basis	beads	450995-5G 450995-25G
Manganese(II) chloride	$MnCl_2$	99.99% trace metals basis	beads	429449-5G 429449-25G
Manganese(II) nitrate hydrate	$Mn(NO_3)_2{\cdot}xH_2O$	99.99% trace metals basis	crystals and lumps	203742-25G 203742-100G
Manganese(II) oxide	MnO	≥99.99% trace metals basis	powder and chunks	431761-1G 431761-10G
Manganese(III) oxide	Mn_2O_3	99.995% trace metals basis	solid	463701-5G 463701-25G
Cobalt(II) carbonate hydrate	$CoCO_3{\cdot}xH_2O$	99.998% trace metals basis	powder	379956-5G
Cobalt(II) chloride	$CoCl_2$	99.999% trace metals basis	beads	409332-1G 409332-5G
Cobalt(II) hydroxide	$Co(OH)_2$	95%	powder	342440-250G
Cobalt(II) nitrate hexahydrate	$Co(NO_3)_2 \cdot 6H_2O$	99.999% trace metals basis	crystals and lumps	203106-10G 203106-50G
Cobalt(II) oxide	CoO	≥99.99% trace metals basis	powder	529443-5G 529443-25G
Nickel carbonate, basic hydrate	$NiCO_3 \cdot 2Ni(OH)_2 \cdot xH_2O$	-	powder	544183-250G-A 544183-1KG-A
Nickel(II) chloride hexahydrate	$NiCl_2 \cdot 6H_2O$	99.999% trace metals basis	crystals and lumps	203866-5G 203866-25G 203866-125G
Nickel(II) chloride	$NiCl_2$	99.99% trace metals basis	powder	451193-5G 451193-25G
Nickel(II) hydroxide	$Ni(OH)_2$	-	powder	283622-5G 283622-250G 283622-1KG
Nickel(II) nitrate hexahydrate	$Ni(NO_3)_2 \cdot 6H_2O$	99.999% trace metals basis	solid	203874-20G 203874-100G 203874-500G
Nickel(II) oxide	NiO	99.999% trace metals basis	solid	481793-5G 481793-25G
Nickel(II) oxide	NiO	99.99% trace metals basis	powder and chunks	203882-20G 203882-100G

Name	Composition	Purity	Form	Prod. No.
Copper(I) chloride	CuCl	≥99.99% trace metals basis	beads	651745-5G 651745-25G
Copper(I) chloride	CuCl	≥99.995% trace metals basis	powder	229628-10G 229628-100G
Copper(II) chloride	$CuCl_2$	99.999% trace metals basis	powder	203149-10G 203149-50G
Copper(II) chloride	$CuCl_2$	≥99.995% trace metals basis	powder	451665-5G 451665-25G
Copper(II) hydroxide	$Cu(OH)_2$	-	powder	289787-250G 289787-1KG
Copper(II) methoxide	$Cu(OCH_3)_2$	97%	solid	332666-5G
Copper(II) nitrate hydrate	$Cu(NO_3)_2 \cdot xH_2O$	99.999% trace metals basis	crystals and lumps	229636-5G 229636-25G 229636-100G
Strontium carbonate	$SrCO_3$	99.995% trace metals basis	powder and chunks	204455-5G 204455-25G 204455-100G
Strontium carbonate	$SrCO_3$	≥99.9% trace metals basis	powder	472018-100G 472018-500G
Strontium chloride hexahydrate	$SrCl_2 \cdot 6H_2O$	99.995% trace metals basis	powder and chunks	204463-10G 204463-50G
Strontium chloride	$SrCl_2$	99.995% trace metals basis	beads	451282-5G
Strontium chloride	$SrCl_2$	≥99.99% trace metals basis	powder	439665-5G 439665-25G
Strontium hydroxide octahydrate	$Sr(OH)_2 \cdot 8H_2O$	99.995% trace metals basis	crystals and lumps	463752-5G 463752-25G 463752-100G
Strontium isopropoxide	$Sr(OCH(CH_3)_2)_2$	99.9% trace metals basis	crystalline powder	440698-5G 440698-25G
Strontium nitrate	$Sr(NO_3)_2$	99.995% trace metals basis	crystals and lumps	204498-10G 204498-50G
Strontium oxide	SrO	99.9% trace metals basis	powder	415138-10G 415138-50G
Niobium(IV) oxide	NbO_2	99.9% trace metals basis	powder	383163-5G
Niobium(V) chloride	$NbCl_5$	99.995% trace metals basis	powder	510696-5G 510696-25G
Niobium(V) chloride	$NbCl_5$	≥99.9% trace metals basis	crystals and lumps	336602-10G 336602-50G
Niobium(V) ethoxide	$Nb(OCH_2CH_3)_5$	99.95% trace metals basis	liquid	339202-5G 339202-50G
Niobium(V) oxide	Nb_2O_5	99.99% trace metals basis	powder	203920-10G 203920-50G 203920-250G
Ruthenium(III) chloride hydrate	$RuCl_3 \cdot xH_2O$	-	powder and chunks	206229-1G 206229-5G 206229-25G
Ruthenium(IV) oxide	RuO_2	99.9% trace metals basis	powder and chunks	238058-1G 238058-5G
Lanthanum(III) oxide	La_2O_3	99.999% trace metals basis	powder	203556-100G
Lanthanum(III) oxide	La_2O_3	99.99% trace metals basis	powder	199923-100G 199923-500G
Lanthanum(III) carbonate hydrate	$La_2(CO_3)_3{\cdot}xH_2O$	99.9% trace metals basis	powder	325767-100G
Lanthanum(III) chloride heptahydrate	$LaCl_3 \cdot 7H_2O$	99.999% trace metals basis	solid	203521-25G 203521-100G
Lanthanum(III) chloride	$LaCl_3$	≥99.99% trace metals basis	beads	449830-5G 449830-25G
Lanthanum(III) hydroxide	$La(OH)_3$	99.9% trace metals basis	powder	447226-50G
Lanthanum(III) nitrate hexahydrate	$La(NO_3)_3 \cdot 6H_2O$	99.999% trace metals basis	solid	203548-25G 203548-100G 203548-500G
Lanthanum(III) nitrate hexahydrate	$La(NO_3)_3 \cdot 6H_2O$	99.99% trace metals basis	solid	331937-5G 331937-100G 331937-500G
Europium(II) chloride	$EuCl_2$	99.99% trace metals basis	powder and chunks	431850-1G 431850-5G
Europium(III) chloride hexahydrate	$EuCl_3 \cdot 6H_2O$	99.99% trace metals basis	crystals and lumps	203254-1G 203254-5G 203254-25G

Name	Composition	Purity	Form	Prod. No.
Europium(III) chloride	$EuCl_3$	99.99% trace metals basis	powder	429732-1G 429732-5G
Europium(III) nitrate hydrate	$Eu(NO_3)_3 \cdot xH_2O$	99.99% trace metals basis	solid	254061-1G 254061-10G
Europium(III) oxide	Eu_2O_3	99.999% trace metals basis	powder and chunks	323543-1G 323543-5G
Europium(III) oxide	Eu_2O_3	99.99% trace metals basis	powder	203262-5G 203262-25G
Bismuth(III) chloride	$BiCl_3$	99.999% trace metals basis	beads	470279-5G 470279-25G
Bismuth(III) chloride	$BiCl_3$	99.999% trace metals basis	powder	450723-5G 450723-25G
Bismuth(III) chloride	$BiCl_3$	99.99% trace metals basis	solid	254142-25G 254142-125G
Bismuth(III) oxide	Bi_2O_3	99.999% trace metals basis	powder	202827-10G 202827-50G 202827-250G
Bismuth(III) oxide	Bi_2O_3	99.9% trace metals basis	powder	223891-100G 223891-500G

Silicides: Promising Thermoelectric Materials


Mikhail I. Fedorov,* Vladimir K. Zaitsev
Ioffe Physical-technical Institute, St. Petersburg, Russia
*Email: m.fedorov@mail.ioffe.ru

Introduction

In recent years, the price of tellurium, a key component in the best-performing thermoelectric materials, has increased significantly, leading to the question, "Is it economically viable to produce thermoelectric generators on an industrial scale?". The main thermoelectric generator material is bismuth telluride, which has a high enough dimensionless figure of merit ($ZT \sim 1$) at room temperature to be practical for energy generating applications. The dimensionless figure of merit is described as:

$$ZT = S^2\sigma T/\kappa$$

where S is the Seebeck coefficient, σ and κ are the electrical and thermal conductivities, respectively, and T is the absolute temperature. The other materials used for higher operating temperatures are PbTe for n-type and GeTe for p-type semiconductors. Both these materials are expensive, especially GeTe. Due to increasing tellurium costs, it is necessary to find alternative materials that have comparable figures of merit.

Silicides represent a group of promising thermoelectric materials, for several reasons: silicon is the fourth most abundant element and among the most widespread elements of the Earth's crust; furthermore, silicides do not contain toxic elements, are ecologically benign, and represent various mechanisms of electron transport. The main characteristics of silicides are presented in **Table 1**, which show the latest results obtained in the field of thermoelectrics.[1,2]

Table 1. Important parameters of several silicide thermoelectrics.[1,2]

Material	Melting Point, *K*	*Eg, eV*	ZT_{max}	ΔS, μ*V/K*
$CrSi_2$*	1763	0.7	0.25 (*p*)	90[3]
$MnSi_{1.7}$	1430	0.66	0.9 (*p*)[8]	100
$FeSi_2$	1490	0.87	0.4 (*n*)[9]; 0.2 (*p*)	70[10]–150[11]
Ru_2Si_3	1970	1.1	0.4 (*n*); 0.3 (*p*)	150 [12]
$ReSi_{1.75}$	2213	0.15	0.8 (*p*)	~450[13]
CoSi	1700	0.016	0.2 (*n*)	-
$Mg_2(Si,Sn)$	1051–1375	0.36–0.77	1.2 (*n*)[4]; 0.5 (*p*)[8]	-

**Eg* for $CrSi_2$ depends strongly on deviation of stoichiometry.[14]

Approaches to Increasing the Thermoelectric Figure of Merit

As shown in the previous equation, the thermoelectric figure of merit is the square of the Seebeck coefficient multiplied by electrical conductivity and divided by thermal conductivity; the result is multiplied by absolute temperature. The Seebeck coefficient and electrical conductivity both depend on charge carrier density and cannot be simultaneously increased in a practical manner. There is an optimum charge carrier density that delivers the highest nominator (power factor) of the thermoelectric figure of merit.

Only one parameter can be changed independently of charge carrier density; this is the thermal conductivity, which consists of two parts—phonon and electron. These parts can be altered more or less independently. The method of creating solid solutions allows significant reductions in thermal conductivity. In this method, the solution of two isovalent materials with the same crystal structure could be used to increase phonon scattering, thereby reducing thermal conductivity. Maximizing ZT requires minimal thermal conductivity.

Another method to increasing the figure of merit is to increase the density of states (DOS). This is very difficult to achieve in some materials, because the density of states is typically dependent only on the band structure of a material, for which there is no means to produce such a change. However, in solid solutions, it is sometimes possible to alter the band structure to increase the figure of merit.

Two Types of Thermoelectric Generators

There are two main types of thermoelectric generators, schematics diagrams for which are shown in **Figure 1**.

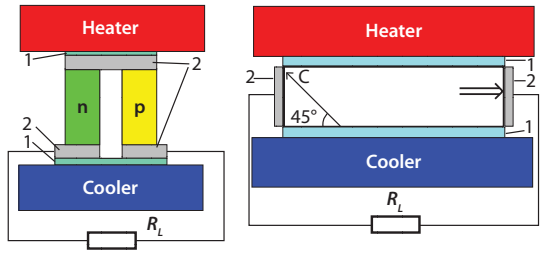

Figure 1. Left) Traditional thermoelement with *n*- and *p*-type legs. Right) Thermo-element with an anisotropic material.

The left scheme shows a traditional thermoelement, consisting of two legs with different types of conductivity (*n* and *p*). The right scheme shows another type of thermoelement, which includes a material with an anisotropic Seebeck coefficient. Here, the voltage of the thermo-element is determined by the difference of longitudinal and transverse Seebeck coefficients. The thermoelectric figure of merit for this case (ZT_a) may be written as:

$$ZT_a = \frac{(S_{\parallel}-S_{\perp})^2\sigma_{\parallel}/\kappa_{\parallel}}{(1+\kappa_{\perp}/\kappa_{\parallel})(1+\sigma_{\parallel}/\sigma_{\perp})}T$$

where symbols || (along the axis of higher symmetry) and ⊥ (across the same axis) denote the direction used to measure this property. In this type of thermoelement, voltage is shown as:

$$V=1/2(S_{\parallel}-S_{\perp})\times\Delta T\times l/d$$

where V - is the voltage of the thermoelement, ΔT is the temperature differential, l - is the length between contacts, and d - is the thickness of the element. Taking into account that ΔT is closely related to the thickness of the element, it is possible to use the following expression for volt/watt sensitivity:

$$V/Q=1/2(S_{||}-S_{\perp})/h/\kappa_{45}$$

where Q is the heat flux through the thermoelement, κ_{45} is the average thermal conductivity at an angle of 45° to the axis of higher symmetry, and h is the width of the strip of thermoelectric material. This formula is valid when contact resistance is much lower than the resistance of the strip. The main advantage of this kind of thermoelement is the absence of contacts in the hot junctions.

Synthesis of Silicides

As discussed previously, silicides are a promising group of nontoxic and cost-efficient materials for thermoelectrics. These materials can be prepared by a variety of methods, particularly those that allow for property measurements. For example, chromium disilicide, higher manganese silicide, ruthenium sesquisilicide, and cobalt monosilicide are prepared by either the Bridgman or Czochralski methods of single crystal preparation. The Czochralski method has also been used for the preparation of rhenium silicide. The floating zone method is also used to synthesize many silicides, especially for refractory types. In laboratory studies of the physical properties of thermoelements, magnesium silicide-based materials are prepared by direct melting of components with subsequent annealing steps.

Transition Metal Silicides

The first five silicides in **Table 1** are referred to as "higher silicides", because they have the maximum silicon content within the corresponding system. With the exception of $CrSi_2$, which crystallizes in a hexagonal structure, all other silicides have crystal structures that are either tetragonal or a slight variant of a tetragonal structure. All of these silicides have high anisotropies of the Seebeck coefficient, making them viable candidates for use in anisotropic thermoelectric generators. As these materials have very large temperature intervals of this anisotropy, they can be used in sensors with high dynamic ranges. Interestingly, in $ReSi_{1.75}$, the anisotropy of Seebeck coefficient is very large; and, in one sample it was found that S was positive, whereas it was negative in another sample, where the direction of the measurement was along the axis of the highest symmetry. These types of applications require each sample to include two Seebeck coefficients with opposite signs, operating in different directions.

The last two silicides in **Table 1** crystallize in a cubic structure. CoSi is almost a semimetal, which allows its use as a contact layer in thermoelectric generators. Cobalt monosilicide has one of the highest power factors of all thermoelectric materials ($N = S^2\sigma$) but a lower overall thermoelectric figure of merit (**Figure 2** and **Figure 3**). Two other silicide materials also have very high power factors. The first is a solid solution of Mg_2Si (Aldrich Prod. No. 343196) and Mg_2Sn, which has $N \sim 45$ W/(mK^2) at 600 K; the other is $CrSi_2$, produced by the synthesis of micron scale powders. In the case of $CrSi_2$, there is some anisotropy of power factor.

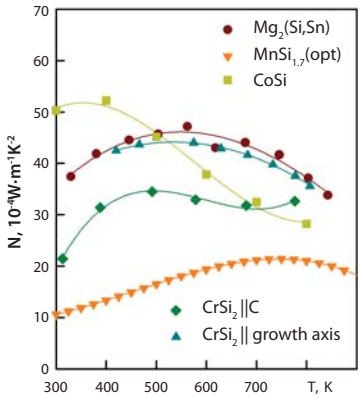

Figure 2. Power factor of some silicides.

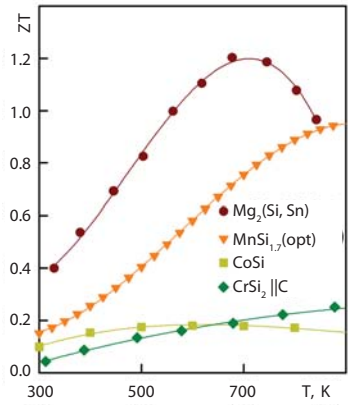

Figure 3. Thermoelectric figure of merit of some silicides.

Interest in the use of chromium disilicide started following an attempt to produce the silicide by high-temperature flux growth in molten tin.[3] Needles formed by this method retained tin within their structure. After etching the tin, the final product contained channels with internal diameters of approximately 100 µm (**Figure 4**). The structural anisotropy is reflected within the varying properties between parallel and perpendicular directions.

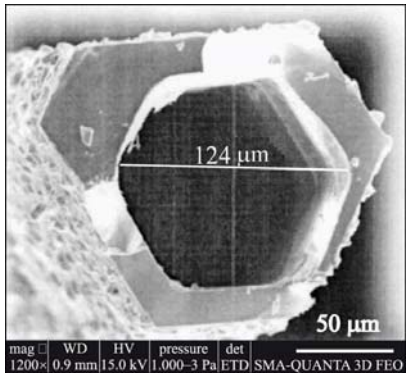

Figure 4. SEM micrograph of $CrSi_2$ tubes obtained from flux growth in molten tin illustrating the hollow interior.

The most efficient thermoelectric material among all transition metal silicides is higher manganese silicide. It has a figure of merit significantly lower than that of Mg_2Si-based materials, but is still in the region of $ZT \sim 0.9$ at 870 K. The best material has to be doped in a complex manner to produce the highest value for figure of merit. The material must contain at least three dopants: one to reduce thermal conductivity, one to optimize the crystalline lattice, and another to optimize the charge carrier density. In an idealized response, the material will have the characteristics shown in **Figure 3** for $Mg_2(Si,Sn)$. In comparison with Mg_2Si-based materials, higher manganese silicide has greater mechanical and chemical strength, which allows its use in air and aggressive media with a limited amount of protection.

Solid Solutions Based on Mg_2Si

The other silicon-based materials are the solid solutions of Mg_2Si and Mg_2Sn.[10] These materials have high thermal conductivities (κ, in W/(m·K); 8.36 Mg_2Si and 6.97 Mg_2Sn) but, in solid solutions, even 10% of the other component reduces thermal conductivity by a significant margin. The conduction band of these compounds consists of two sub-bands located in the *X*-point of the Brillouin zone. The lower band of Mg_2Si consists of the states of Si, whereas the lower band of Mg_2Sn consists of the Mg states. The change of position of the sub-bands allows for an increased density of states in the conduction band. There are therefore two mechanisms to increase the figure of merit in solid solutions based on Mg_2Si and Mg_2Sn. It is possible to reduce the thermal conductivity and, within the region of lower thermal conductivity, to find the optimum position of the sub-bands.

There are two optimum impurities which allow control of the charge carrier density—Bi and Sb. Both impurities work well to optimize the density, but the mechanical properties of material doped with Bi are slightly better. As shown in **Figure 5**, the results of the present study are very similar to those previously reported by Isoda *et al.*[12,13] and Zhang *et al.*[14]

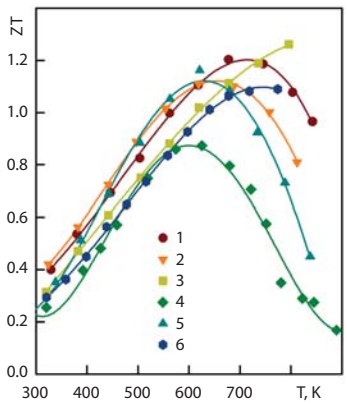

Figure 5. Figures of merit for solid solutions of Mg_2Si and Mg_2Sn. 1) $Mg_2Si_{0.4}Sn_{0.6}$ <Sb>;[10] 2) $Mg_2Si_{0.4}Sn_{0.6}$ <Bi>;[10] 3) $Mg_2Si_{0.36}Ge_{0.04}Sn_{0.6}$;[10] 4) $Mg_2Si_{0.5}Sn_{0.5}$;[12] 5) $Mg_2Si_{0.5}Sn_{0.5}$;[13] 6) $Mg_2Si_{0.4}Sn_{0.6}$.[14]

In this system, it is difficult to produce a *p*-type material with a $ZT > 0.5$,[4] due to the position of the valence band in the *Γ*-point of the Brillouin zone and a relatively low energy gap in Mg_2Sn.

Conclusions

Thermoelectrical research could benefit greatly from a single rule to determine the most appropriate material for a given application. Unfortunately, no such method exists, so all cases require examination of the interactions between many parameters, and it is not always possible to determine the optimal material constituents.

As shown above, the higher transition metal silicides are very well-suited for anisotropic thermoelectric conversion. Essential anisotropy of Seebeck coefficient, together with good mechanical properties, allows production of reliable anisotropic thermoelectric converters.

For traditional thermoelectric modules, the situation is different. There is no coupling of the materials that have high *ZT* values for both signs. In this case, it is necessary to produce a thermoelectric generator comprising significantly different materials that may result in the device having low reliability.

References

(1) Fedorov, M. I.; Zaitsev, V. K. *Thermoelectrics Handbook. Macro to Nano*; Rowe, D. M., Ed.; CRC press. Taylor & Francis group, Boca Raton-London-New York, **2006**; pp 31-1-31-19.
(2) Zaitsev, V. K.; Fedorov, M. I.; Eremin, I. S.; Gurieva, E. A. *Thermoelectrics Handbook. Macro to Nano*; Rowe, D. M., Ed.; CRC press. Taylor & Francis group, Boca Raton-London-New York, **2006**; pp 29-1-29-11.
(3) Solomkin, F. Yu.; Suvorova, E. I.; Zaitsev, V. K.; Novikov, S. V.; Burkov, A. T.; Samunin, A. Yu.; Isachenko, G. N. *Tech. Phys.* **2011**, *81*, 147.
(4) Fedorov, M. I.; Zaitsev, V. K.; Isachenko, G. N. *Solid State Phenomena*, **2011**, *170*, 286.
(5) Hesse, J. *Z. Angew. Phys.* **1969**, *28*, 133.
(6) Takeda, M.; Kuramitsu, M.; Yoshio, M.; *Thin Solid Films* **2004**, *461*, 179.
(7) Andreev, A. A.; Fedorov, M. I.; Ivanov, Yu.V.; Petrova, V.S.; Zaitsev, V. K. *J. of Electronic Mater.* **2011**, *40*, 1485.
(8) Simkin, B. A.; Hayashi, Y.; Inui H. *Intermetallics*, **2005**, *13*, 1225.
(9) Gu, J.-J.; Oh, M.-W.; Inui, H.; Zhang, D. *Phys. Rev. B*, **2005**, *71*, 113201.
(10) Zaitsev, V. K.; Fedorov, M. I.; Gurieva, E. A.; Eremin, I. S.; Konstantinov, P. P.; Samunin, A. Yu.; Vedernikov, M. V. *Phys. Rev. B.* **2006**, *74*, 045207.
(11) Voronov, B. K.; Dudkin, L. D.; Trusova, N. N. Chemical bond in semiconductors, **1969**, pp 291-298 (in Russian).
(12) Isoda, Y.; Nagai, T.; Fuziu, H.; Imai, Y.; Shinohara, Y. *Proceedings of ICT'06* **2006**, IEEE, pp 406.
(13) Isoda, Y.; Nagai, T.; Fujiu, H.; Imai, Y.; Shinohara Y. *Proceedings of ICT'07* **2008**, IEEE, pp 251.
(14) Zhang, Q.; He, J.; Zhu, T. J.; Zhang, S. N.; Zhao, X. B.; Tritt, T. M. *Appl. Phys. Lett.* **2008**, *93*, 102109.

Metal Silicides for Thermoelectric Applications

For a complete list of available materials, visit Aldrich.com/silicides

Name	Composition	Purity	Form	Prod. No.
Iron disilicide	$FeSi_2$	99.9%	powder	752622-5G
Magnesium silicide	Mg_2Si	99.99%	pieces	752630-5G
Molybdenum disilicide	$MoSi_2$	≥99.8% trace metals basis	powder	752290-25G
Chromium disilicide	$CrSi_2$	99.9% trace metals basis	powder	752304-25G
Magnesium silicide	Mg_2Si	≥99% trace metals basis	powder	343196-25G

Chalcogenide Thermoelectric Materials

For a complete list of available materials, visit Aldrich.com/chalcogenides

Name	Composition	Purity	Form	Prod. No.
Bismuth antimony telluride	$Bi_{0.5}Sb_{1.5}Te_3$	99.99% trace metals basis	beads	752509-5G
Bismuth(III) telluride	Bi_2Te_3	99.99%	beads	751421-5G
Tin(II) selenide	SnSe	99.99%	crystals	751448-5G
Tin(II) sulfide	SnS	≥99.99%	granular	741000-5G
Antimony(III) telluride	Sb_2Te_3	99.96% trace metals basis	powder	733490-1G
Antimony(III) telluride	Sb_2Te_3	≥99.99%	beads	740993-5G
Bismuth(III) telluride	Bi_2Te_3	99.99% trace metals basis	powder	733482-5G
Antimony(III) selenide	Sb_2Se_3	99.99% trace metals basis	solid	401196-5G
Bismuth selenide	Bi_2Se_3	99.999% trace metals basis	granular (melted)	733504-5G
Bismuth(III) selenide	Bi_2Se_3	-	solid	401080-5G
Lead(II) telluride	PbTe	99.998% trace metals basis	crystals and lumps	254266-50G
Silver(I) telluride	Ag_2Te	-	powder and chunks	400645-5G

Materials for Synthesis of Silicides

For a complete list of available materials, visit Aldrich.com/metals

Name	Composition	Purity	Form	Prod. No.
Magnesium	Mg	99.98% trace metals basis	chips	254118-250G 254118-1KG
Magnesium	Mg	99.998% trace metals basis	dendritic pieces	474754-5G 474754-25G
Magnesium	Mg	99.99% trace metals basis	dendritic pieces	465992-5G 465992-25G
Magnesium	Mg	≥99.9% trace metals basis	rod	299405-10G
Magnesium	Mg	99.95% trace metals basis	turnings	403148-50G 403148-250G
Magnesium	Mg	≥99% trace metals basis	ingot	735779-1EA
Silicon	Si	99.95% trace metals basis	pieces	343250-50G 343250-500G
Silicon	Si	99.999% trace metals basis	powder	267414-25G
Silicon	Si	99% trace metals basis	powder	215619-50G 215619-250G 215619-1KG
Chromium	Cr	99.95%	grit	27066-500G-F
Chromium	Cr	99.995% trace metals basis	chips	374849-50G 374849-250G
Manganese	Mn	99%	chips	266167-500G
Manganese	Mn	99.99% trace metals basis	powder	463728-25G 463728-100G
Iron	Fe	99.98% trace metals basis	chips	267945-250G 267945-1KG
Iron	Fe	99.995% trace metals basis	granular	413054-5G 413054-25G
Iron	Fe	≥99.99% trace metals basis	powder	255637-10G 255637-50G

Name	Composition	Purity	Form	Prod. No.
Iron	Fe	≥99.9% trace metals basis	powder	267953-5G 267953-250G 267953-1KG
Iron	Fe	99.98% trace metals basis	rod	266213-30G 266213-150G
Iron	Fe	≥99.99% trace metals basis	wire	266256-3.1G 266256-15.5G
Germanium	Ge	99.999% trace metals basis	chips	263230-10G 263230-50G
Germanium	Ge	99.999% trace metals basis	chips	203343-1G 203343-5G 203343-25G
Germanium	Ge	≥99.999% trace metals basis	powder	327395-5G 327395-25G
Germanium	Ge	≥99.99% trace metals basis	powder	203351-10G 203351-50G
Ruthenium	Ru	99.99% trace metals basis	powder	545023-1G 545023-5G
Ruthenium	Ru	99.9% trace metals basis	powder	209694-5G
Rhenium	Re	99.995% trace metals basis	powder	204188-5G
Rhenium	Re	99.99% trace metals basis	rod	449482-6.9G
Rhenium	Re	≥99.9% trace metals basis	wire	357111-200MG
Tin	Sn	-	granular	14507-100G-R 14507-250G-R 14507-6X250G-R 14507-1KG-R 14507-6X1KG-R
Tin	Sn	99.999%	bars	265659-100G 265659-250G
Tin	Sn	99.8% trace metals basis	powder	265632-100G 265632-500G
Tin	Sn	99.999% trace metals basis	shot	204692-10G
Tin	Sn	99.999% trace metals basis	wire	356956-7G

ALDRICH Materials Science

Hard Materials Center of Excellence

Custom Research Services

The Hard Materials Center of Excellence at Urbana, Illinois, addresses a variety of technologies ranging from Alternative Energy and Electronics to Biomedical applications. Research and development capabilities available at the Center enable development and custom manufacturing of high-purity metals, alloys, salts, advanced ceramics and other hard materials.

The Hard Materials Center of Excellence offers:

- Forming and shaping of metals
- Purification of metals by vacuum distillation
- Purification of high-purity salts by crystallization
- Synthesis and packaging in controlled/inert-gas atmosphere
- Full analytical suite including XRD, particle size analysis, ICP-MS/OES, DSC/TGA, elemental analysis, NMR and more
- High-temperature solid-state synthesis
- Processing and purification of rare earth metals

Examples of Custom Capabilities

- Filling crucibles for molecular beam epitaxy (MBE)
- Preparation of metal alloys and composites
- Synthesis of complex oxides and ceramics
- Beading of metals and and high-purity metal salts

To inquire about our custom capabilities, contact us at **HardMaterials@sial.com**

Combinatorial Materials Science for Energy Applications

R. Bruce van Dover
Department of Materials Science and Engineering
Cornell University
Ithaca, NY 14853-1501
Email: rbv2@cornell.edu

Introduction: The Role of Combinatorial Materials Science

Materials are the fundamental basis for solutions to the most pressing issues in energy generation, transport, and utilization, as well as more general issues in sustainability. In many cases, long-term solutions to these problems will depend on breakthrough innovations in materials. As emphasized by the U.S. Department of Energy panel on "New Science for a Secure and Sustainable Energy Future":

"…existing energy approaches-even with improvements from advanced engineering and improved technology based on known concepts will not be enough to secure our energy future. Instead, meeting the challenge will require new technologies for producing, storing and using energy with performance levels far beyond what is now possible. Such technologies spring from scientific breakthroughs in new materials and chemical processes that govern the transfer of energy between light, electricity and chemical fuels."[1]

Can there be an effective strategy for finding breakthrough materials, since they are, by definition, unpredictable?

One answer is found in Combinatorial Materials Science techniques, which represent a powerful approach to identifying new and unexpected materials. The high cost of single-sample synthesis/characterization, along with the need for reduced research and development time are driving the materials community to explore high-throughput methodologies. Increasing the number of materials that are studied can increase the understanding of composition/property relationships and the probability of a breakthrough materials discovery. To be effective, this method must balance the need for robust and authoritative measures of properties with the need for rapid characterization.

Figure 1 delineates some of the considerations that must be met for the high-throughput synthesis/characterization approach to be viable. It is not necessary that materials made by the chosen high-throughput synthesis technique be identical to those made in one-off experiments, but it is necessary that the resulting properties are similar. Materials properties depend on morphology, microstructure and other process-dependent variables. Thin films are often particularly convenient to work with and sometimes have properties that differ significantly from their bulk counterparts. Fortunately, it is found, in many cases, that compositional trends observed in thin films closely approximate those of the bulk.

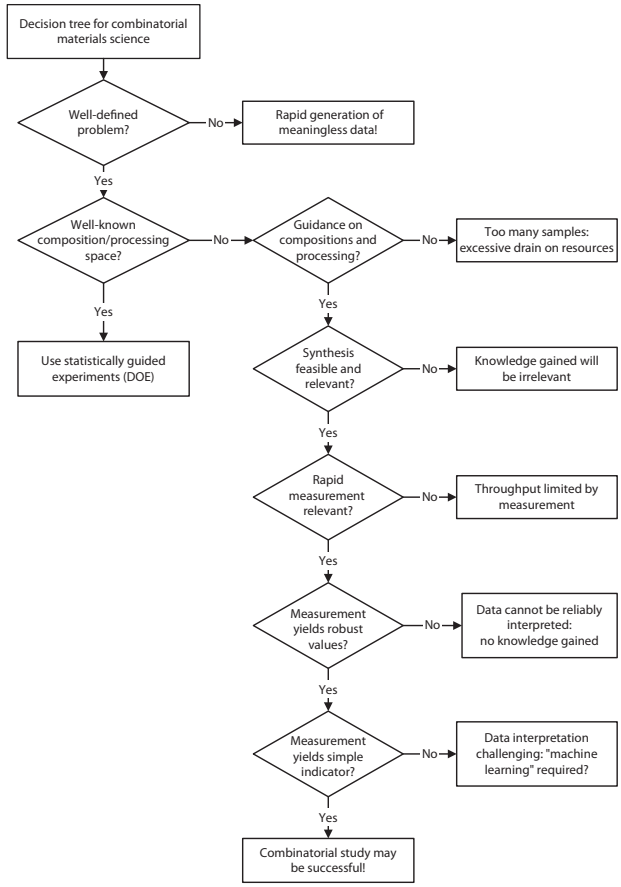

Figure 1. Is the combinatorial/high-throughput approach the right choice to find a new material that can solve an outstanding problem? This decision tree illustrates some of the key questions that should be asked. When the right conditions are met, high-throughput experiments can be impressively effective.

Many methods for high-throughput synthesis have been developed,[2,3] but the Codeposited Composition Spread (CCS) technique has proven to be an especially versatile method for forming a wide range of compositions in a single experiment. In this method, thin films are deposited by physical vapor deposition on a substrate simultaneously, from two or more sources that are spatially separated and chemically distinct, producing a film with an inherent composition gradient and intimate mixing of the constituents. With three sources, an entire ternary phase diagram may be produced in a single experiment.

Composition spreads may also be synthesized using a traveling shutter[4] or shaped mask[5] to create a film with a thickness gradient (wedge). A composition gradient can then be obtained by rotating the sample with respect to the shutter and depositing a new overlapping wedge of a second or third film. Atomic mixing is achieved by depositing many wedges each of submonolayer thickness. This approach has the advantage of the composition/position dependence being well-defined (ignoring resputtering effects), although surface reorganization during the short time between wedge depositions can lead to adventitious artifacts.

CCS synthesis is distinct from conventional "combinatorial chemistry" as employed, for example, in drug discovery[6] as well as the discrete combinatorial synthesis (DCS) approach pioneered by Xiang and Schultz.[7] In the latter, mixtures of inorganic components are created by sequential deposition of discrete layers of precursors followed by moderate- or high-temperature diffusion and reaction steps. An important advantage of the DCS technique is that arbitrary compositions with a large number of constituents can be prepared as desired. A key advantage of the composition-spread approach is the opportunity to prepare materials with no subsequent processing, which means that low-temperature or metastable phases may be prepared. The CCS approach also allows properties to be determined with very fine composition resolution, often limited by the resolution of the property measurement itself. For example, it is generally straightforward to sample composition space at 1 mol% intervals, equivalent to investigating thousands of materials in a single experiment. The CCS technique has been used to create both alloys and compounds in chemical systems, including intermetallics, nitrides, oxides, and carbides. A large number of thin film deposition techniques are available for synthesis of composition spread thin films, including evaporation,[8,9] sputtering,[10-12] pulsed-laser deposition (PLD),[13] chemical vapor deposition,[14] and cold-plasma processing,[15] among others. Of these, sputtering offers a unique combination of advantages:

- In most cases sputtering rates are constant and reproducible[16] when powered by modern dc, rf, or pulsed-dc regulated power supplies, allowing composition spreads with a targeted range of compositions to be synthesized.
- When magnetron sputter guns are used for sputtering there is little interaction between the sources. That is, the deposition rate from one gun is independent of the operation of the other guns. As a result the composition profile (composition of the codeposited film as a function of position on the substrate) can be predicted quantitatively once the deposition rate for each individual source is determined. However, in some circumstances the magnetron gun may interact significantly with the growing films, leading to resputtering and deviation of the composition from that predicted by simple summation of independent deposition rates. This effect can be predicted quantitatively using known sputter yields and the conditions of the sputter system, leading to accurate adjustments and an excellent quantitative prediction of the composition.
- The composition gradients achieved by codeposition (using two-inch-diameter sources) are typically about 1 atomic percent per mm, a convenient scale that allows many measurement techniques to resolve trends with about 1 atomic percent resolution.
- Sputtering is convenient for deposition of metals, oxides (by reactive sputtering in an oxygen-containing ambient), nitrides (sputtering in Ar-N_2), carbides (sputtering Ar-CH_4), and mixed anion (e.g., oxynitride) systems. Targets of most metals and many unary and binary oxides are readily available, along with many other common materials.

Sputter codeposition also has inherent disadvantages, including:

- It is not simple to change the composition gradient. The gradient is affected by changing the total inert gas pressure in the system, but many other aspects of sputtering change as well, confounding systematic studies.
- Targets of the alkali metals, alkaline earth metals, and the lighter lanthanide metals are problematic, due to rapid oxidation/hydrolysis/hydration of the metal target in air.

Determining the structure of the materials formed in a composition spread is important for understanding composition/property relations. Thin films are well suited for X-ray diffraction studies for phase identification. Using automated data acquisition, in either a conventional stationary-anode diffractometer[17] or a synchrotron-based system,[18] hundreds of diffraction patterns can be acquired on a single composition-spread substrate. An unsolved challenge is to develop automated techniques for the identification of unique diffraction patterns and clustering these into contiguous phase fields corresponding to regions (compositions) of the CCS film. Some progress has been made in this respect,[17,19] but a fully robust algorithm has yet to be developed.

Fuel Cell Studies

Combinatorial techniques have been used in a wide range of energy-related studies, both to identify new higher-performance materials and to elucidate the composition-dependent properties of known systems. One challenge for which the CCS technique has been found to be particularly well-suited is that of identifying superior electrocatalysts for Polymer Electrolyte Membrane (PEM) fuel cells.[20] Catalysis is a complex phenomenon that is essentially impossible to predict with confidence; incremental improvements may be obtained using rational design, but the only way to identify new active compositions is by screening a large number of compositions. Mallouck and coworkers[20] developed a viable technique for qualitative optical screening of catalytic activity, which has been further developed into a semiquantitative method.[21] Alternative methods for identifying active materials include multiple independent electrode arrangements[22] and scanning electrochemical microscopy.[23]

As an illustrative example, the CCS technique was recently used to gain insight into the most catalytically active material in the Pt-Ta and related systems. After exploring hundreds of chemical systems, the Pt-Ta system was identified as showing interesting activity, and it was selected for close study of the onset potential for methanol oxidation determined by optical fluorescence as a function of position on the binary composition spread. X-ray diffraction data was collected in a high-throughput automated experiment using a synchrotron beamline and used to identify phase fields, as illustrated in **Figure 2**. It was immediately clear that the best catalyst behavior (lowest value for the half-wave potential $E_{1/2}$) is strongly correlated with the presence of the orthorhombic Pt_2Ta structure, and that the activity is optimized at the approximately stoichiometric composition $Pt_{0.71}Ta_{0.29}$.[24]

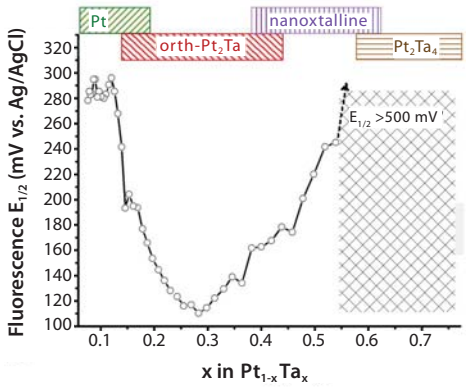

Figure 2. The catalytic activity of Pt-Ta compositions is measured using a fluorescence test: a lower half-wave potential, $E_{1/2}$, implies greater activity for methanol oxidation. This plot shows that strong activity is associated with the presence of the orthorhombic Pt_2Ta phase, is best in the single phase region (18 -35 at% Ta), and is optimized at the composition $Pt_{0.71}Ta_{0.29}$, close to the stoichiometric value.[24]

Figure 2 shows that the fine compositional resolution offered by the CCS technique permits two important conclusions about the internal consistency of the data. First, the close agreement between values at adjacent compositions indicates that random variations in the measurement are small compared to the overall trend. Second, the smooth trend with composition in the Pt_2Ta phase field allows the optimum composition to be identified with confidence. Internal consistency does not prove that the data is accurate in composition or in $E_{1/2}$ value; the absolute accuracy must be validated by comparison

with detailed one-off studies. The key advantage of the combinatorial method is that it allows the researcher to efficiently identify particular compositions for further study based on data rather than on conservative or radical speculation.

Predicting catalytic properties is not reliable—neither from first principles nor from accumulated experience—so catalyst development has always relied on an empirical approach. High-throughput studies have proven especially useful in facilitating rapid optimization of catalyst composition using factorial designs as well as more exotic approaches, such as genetic algorithms.[25] Solution-based synthesis is often employed for optimization because it most closely approximates the processing of realistic formulations. The high-throughput approach has been applied successfully to primary screening and optimization for a wide range of catalyst functions, including polymerization catalysts, enantioselective catalysts, oxidation catalysts, reduction catalysts, dehydrogenation catalysts, and many others.

Transparent Conductivity Oxides

Another example of the usefulness of the combinatorial materials science approach is provided in the study of transparent conducting oxides-materials that serve a wide range of energy-related optoelectronic functions, from low-emissivity window coatings to frontside current collectors in photovoltaics.[26,27] Established *n*-type transparent oxides, such as $In_{1-x}Sn_xO_y$, SnO_2:F, and ZnO:Al, offer adequate performance, but with concomitant drawbacks, such as low thermal stability or high cost. More complex materials based on Ga_2O_3 (Aldrich Prod. No. 215066), SnO_2 (Aldrich Prod. No. 518174), ZnO (Aldrich Prod. No. 204951), CdO (Aldrich Prod. No. 202894), and In_2O_3 (Aldrich Prod. No. 203424) and their multinary mixtures offer the prospect of improved performance and have been the subject of high-throughput as well as conventional studies.

ZnO is an inexpensive wide-bandgap semiconductor with excellent optical transmission. Highly conductive *n*-type ZnO has been achieved through doping with Al, In, or Ga. The electrical properties of ZnO are highly dependent on native point defects such as oxygen vacancies, zinc interstitials, and hydrogen, all of which act as electron donors. In order to obtain high conductivity ZnO, these point defects must be deliberately induced by doping. The highest conductivity is achieved after annealing in reducing conditions, while exposure to oxidizing conditions (typically air at moderate temperatures) degrades the conductivity significantly. Extensive studies on the substitution of Al^{3+} on the Zn^{2+} site have shown that doping at the level of a few atomic percent leads to a moderately high conductivity that is fairly stable. Doping with In^{3+} has a similar effect. Since Al^{3+} has an ionic radius 32% smaller than that of Zn^{2+}, and In^{3+} has an ionic radius 9% larger, it is not surprising to find that the introduction of either impurity degrades the electron mobility of ZnO. A composition spread study of the conductivity, mobility, and crystal structure of the (Zn, Al, In, O) system allowed the effect of these impurities to be clarified. **Figure 3** shows that codoping with both Al and In degraded mobility less than doping with either element alone.[28] The lattice strain inferred from x-ray diffraction shows a similar trend; the average lattice constant matches that of undoped ZnO for materials with the highest mobility. The conductivity is also maximum for this condition. Use of a composition spread sample allowed the experiment to be executed without the confounding associated with typical run-to-run variations that accompany one-off studies, thereby allowing robust conclusions to be drawn.

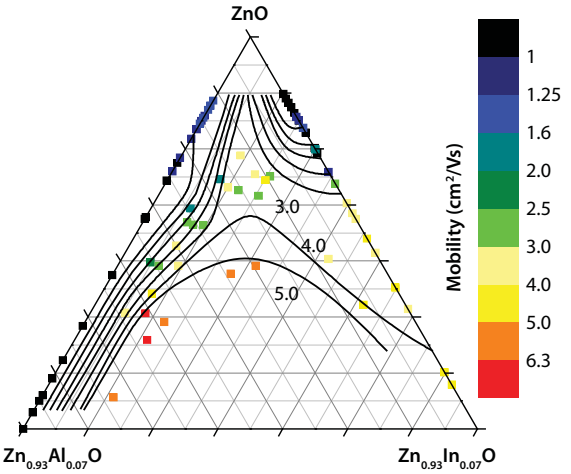

Figure 3. ZnO with Al or In forms a transparent conductor. Compared to Zn^{2+}, the Al^{3+} ion is much smaller while In^{3+} is much larger. Co-doping yields an "average" dopant size that is a better fit in the ZnO crystal, reducing scattering. A Zn-Al-In-oxide composition spread allows the effect of varying levels of both dopants to be measured. The binary spreads Zn-Al-oxide and Zn-In-oxide are prepared in separate experiments under nominally identical conditions. For a given overall doping level, the highest mobility is observed in co-doped compositions.[28]

Other Energy-related Studies

Combinatorial materials science techniques have great potential for many other studies of energy-related materials. Thermoelectrics offer the potential to revolutionize technologies such as high energy refrigeration or energy scavenging from low-grade heat sources, a prospect that has driven the search for a breakthrough in thermoelectric materials.[29] Many of the ingredients needed for a successful combinatorial search are in place. There is a well-accepted Figure of Merit (FOM) for thermoelectric materials that can, in principle, be measured in a thin film geometry. Recent concepts regarding the factors that might lead to high FOM materials could provide guidance regarding materials systems worthy of investigation.[30] Perhaps the most challenging aspect of a search for new thermoelectrics is the sensitivity of the thermoelectric FOM to doping, which implies that a suitable dopant introduced at the optimum concentration must be identified for any prospective candidate. This both increases the number of materials combinations dramatically and introduces the possibility of strong sensitivity to process conditions.

Another example is that of piezoelectric materials, which have a variety of commercial applications and are proving useful in harvesting low-grade energy. Only a small number of piezoelectric materials are commonly used: others are known but barely characterized. Undoubtedly, many more have yet to be synthesized or characterized. Highly-textured crystalline thin films are needed for reliable characterization of piezoelectric properties, so microstructure control may be a key synthesis issue. Screening approaches should be straightforward, using optical techniques or atomic force microscope (AFM) cantilever probing. New phases, perhaps with a wider processing window or larger piezoelectric Figure of Merit, could be quite exciting, both from a fundamental point of view as well as from the perspective of commercial importance.

Outstanding Issues

While development of synthesis and characterization techniques is basic to the concept of high-throughput experimentation, these steps lead to data and information, not knowledge or insight. In fact, the massive quantity of data, coupled with the modest level of accuracy or precision associated with the speed/quality tradeoff, quickly leads to a new challenge-how to make use of the data. Tracking only the latest top-performing material in a high-throughput investigation discounts the insights and new directions that could be gleaned from lesser-performing materials.

Efficient methods are urgently needed for transforming an over-whelmingly data-rich environment into actionable insights regarding structure-processing-property associations and relationships in materials. Machine learning and statistical approaches, such as cluster analysis and multivariate regression, are important components for this task, but they do not incorporate the relationships that are inherent in the physics and chemistry of materials. Thus, perhaps the most essential difference between conventional research and the combinatorial materials science approach is in the role of informatics—the processing, management and retrieval of information.

Conclusions

The high-throughput approach to inorganic materials discovery improves the likelihood of discovering new materials with useful properties because it dramatically lowers the cost—in terms of financial resources, human effort, and time—of examining unexplored regions of composition space, including regions that might be avoided as unlikely candidates for an expensinve one-off study. Experience has shown that high-throughput screening can be a useful tool for solving real-world problems in materials discovery if three broad criteria are met: In general, the approach is suitable for a well-defined problem for which samples can be prepared using parallelized synthesis and evaluated using a suitable high-throughput screen. High-throughput techniques are also valuable for investigations of known materials systems, where the goal is to elucidate the composition dependence of materials properties. The codeposited composition spread technique has proven particularly effective for exploring energy-related materials in a wide range of investigations.

Acknowledgments

This work was supported by the U.S. Department of Energy (DOE), Office of Science, Office of Basic Energy Sciences (under Award Number DE-FG02-07ER46440). The author would like to gratefully acknowledge formative discussions with Lynn Schneemeyer, Héctor Abruña, Francis DiSalvo and John Gregoire.

References

(1) Hemminger, J.; Crabtree, G. W.; Kastner, M. "New science for a secure and sustainable energy future," Office of Basic Energy Sciences, Department of Energy, 2008.
(2) Xiang, X.-D.; Takeuchi, I., Eds. *Combinatorial Materials Synthesis*; Marcel Dekker: New York, 2003.
(3) *High-throughput Synthesis: Principles and Practices*; Marcel Dekker: New York, 2001.
(4) Xiang, X.-D. *Bull. Am. Phys. Soc.* **1999**, *44*, 103.
(5) Dahn, J. R.; Trussler, S.; Hatchard, T. D.; Bonakdarpour, A.; Mueller-Neuhaus, J. R.; Hewitt, K. C.; Fleischauer, M. *Chem Mater* **2002**, *14*, 3519.
(6) Doyle, P. M. *J Chem. Tech.* **1995**, *64*, 317.
(7) Xiang, X.-D.; Sun, X.; Briceno, G.; Lou, Y.; Wang, K.-A.; Chang, H.; Wallace-Freedman, W. G.; Chen, S.-W.; Schultz, P. G. *Science* **1995**, *268*, 1738.
(8) Kennedy, K.; Stefansky, T.; Davy, G.; Zackay, V.; Parker, E. R. *J Appl Phys* **1965**, *36*, 3808.
(9) Hammond, R. H.; Ralls, K. M.; Meyer, C. H.; Snowden, D. P.; Kelly, G. M.; Pereue, J. H., Jr. *J. Appl. Phys.* **1971**, *43*, 2407.
(10) Hanak, J. J. *J. Mat. Science* **1970**, *5*, 964.
(11) van Dover, R. B.; Hong, M.; Gyorgy, E. M.; Dillon, J. F., Jr.; Albiston, S. D. *J Appl Phys* **1985**, *57*, 3897.
(12) van Dover, R. B.; Schneemeyer, L. F.; Fleming, R. M. *Nature (UK)* **1998**, 162.
(13) Lippmaa, M.; Koida, T.; Minami, H.; Jin, Z. W.; Kawasaki, M.; Koinuma, H. *Applied Surface Science* **2002**, *189*, 205.
(14) Smith, R. C.; Hoilien, N.; Roberts, J.; Campbell, S. A.; Gladfelter, W. L. *Chem Mater* **2002**, *14*, 474.
(15) Terajima, T.; Koinuma, H. *Applied Surface Science Proceedings of the Second Japan-US Workshop on Combinatorial Materials Science and Technology* **2004**, *223*, 259.
(16) Gregoire, J. M.; Dale, D.; Kazimirov, A.; DiSalvo, F. J.; van Dover, R. B. *Journal of Vacuum Science & Technology A* **2010**, *28*, 1279.
(17) Long, C. J.; Hattrick-Simpers, J.; Murakami, M.; Srivastava, R. C.; Takeuchi, I.; Karen, V. L.; Li, X. *Review of Scientific Instruments* **2007**, *78*.
(18) Gregoire, J. M.; Dale, D.; Kazimirov, A.; DiSalvo, F. J.; van Dover, R. B. *Review of Scientific Instruments* **2010**, *80*, 123905.
(19) Long, C. J.; Bunker, D.; Li, X.; Karen, V. L.; Takeuchi, I. *Review of Scientific Instruments* **2009**, *80*.
(20) Reddington, E.; Sapienza, A.; Gurau, B.; Viswanathan, R.; Sarangapani, S.; Smotkin, E. S.; Mallouk, T. E. *Science* **1998**, *280*, 1735.
(21) Gregoire, J. M.; Kostylev, M.; Tague, M. E.; Mutolo, P. F.; van Dover, R. B.; DiSalvo, F. J.; Abruna, H. D. *J Electrochem Soc* **2009**, *156*, 160.
(22) Strasser, P.; Fan, Q.; Devenney, M.; Weinberg, W. H.; Liu, P.; Norskov, J. K. *Journal of Physical Chemistry B* **2003**, *107*, 11013.
(23) Jayaraman, S.; Hillier, A. C. *Journal of Physical Chemistry B* **2003**, *107*, 5221.
(24) Gregoire, J. M.; Tague, M. E.; Cahen, S.; Khan, S.; Abruna, H. D.; DiSalvo, F. J.; van Dover, R. B. *Chem Mater* **2009**, *22*, 1080.
(25) Potyrailo, R. A.; Maier, W. F., Eds. *Combinatorial and High-Throughput discovery and Optimization of Catalysts and Materials*; Taylor & Francis: Boca Raton, 2007.
(26) Ginley, D. S.; Bright, C. *MRS Bulletin* **2000**, *25*, 15.
(27) Perkins, J. D.; del Cueto, J. A.; Alleman, J. L.; Warmsingh, C.; Keyes, B. M.; Gedvilas, L. M.; Parilla, P. A.; To, B.; Readey, D. W.; Ginley, D. S. In *2nd International Symposium on Transparent Oxide Thin Films for Electronics and Optics (TOEO-2), 8-9 Nov. 2001*; Elsevier: Switzerland, 2002; Vol. 411, pp 152.
(28) Kirby, S. D.; van Dover, R. B. *Thin Solid Films* **2009**, *517*, 1958.
(29) DiSalvo, F. J. *Science* **1999**, *285*, 703.
(30) Mahan, G. D. *J Appl Phys* **1989**, *65*, 1578.

Sputtering Targets and Pellets

For a complete list of available materials, visit Aldrich.com/renewable

Name	Composition	Purity	Dimensions	Prod. No.
Aluminum zinc oxide	Al_2O_3	99.99% trace metals basis	diam. × thickness 3.00 × 0.125 in.	752665-1EA
Gallium zinc oxide	Ga_2O_3	99.99% trace metals basis	diam. × thickness 3.00 × 0.125 in.	752673-1EA
Indium zinc oxide	In_2O_3	99.99% trace metals basis	diam. × thickness 3.00 × 0.125 in.	752703-1EA
Indium tin oxide	InSnO	99.99% trace metals basis	diam. × thickness 3.00 × 0.125 in.	752657-1EA
Zinc oxide	ZnO	99.99% trace metals basis	diam. × thickness 3.00 × 0.125 in.	752681-1EA
Indium oxide	In_2O_3	99.99% trace metals basis	diam. × thickness 3.00 × 0.125 in.	752649-1EA
Zinc	Zn	99.995% trace metals basis	diam. × thickness 3.00 × 0.125 in.	749060-1EA
Chromium	Cr	99.95% trace metals basis	diam. × thickness 3.00 × 0.125 in.	749052-1EA
Titanium	Ti	99.995% trace metals basis	diam. × thickness 3.00 × 0.125 in.	749044-1EA

Name	Composition	Purity	Dimensions	Prod. No.
Cerium(IV) oxide-samarium doped	CeO_2	-	diam. × L 2-3 × 3-5 mm	734675-10G
Cerium(IV) oxide-gadolinium doped	CeO_2	-	diam. × L 2-3 × 3-5 mm	734667-10G
Zirconium(IV) oxide-yttria stabilized	$ZrO_2 \cdot Y_2O_3$	-	diam. × H 2-3 × 3-5 mm	734683-10G

High-purity Metal Foils for Physical Vapor Deposition

For a complete list of available materials, visit Aldrich.com/metals

Name	Composition	Purity	Dimensions	Prod. No.
Aluminum	Al	99.999% trace metals basis	thickness 1.0 mm	266957-27.2G
Aluminum	Al	99.999% trace metals basis	thickness 0.5 mm	266574-3.4G 266574-13.6G
Aluminum	Al	99.999% trace metals basis	thickness 0.25 mm	326852-1.7G 326852-6.8G
Aluminum	Al	99% trace metals basis	L × W 150 × 150 mm thickness 8 µm	733369-4EA
Titanium	Ti	99.99% trace metals basis	thickness 0.5 mm	348805-1.4G
Titanium	Ti	99.99% trace metals basis	thickness 0.25 mm	267481-700MG
Titanium	Ti	99.99% trace metals basis	thickness 0.1 mm	348813-280MG 348813-1.1G
Titanium	Ti	99.98% trace metals basis	thickness 0.025 mm	348848-280MG 348848-1.1G
Vanadium	V	99.7% trace metals basis	thickness 0.127 mm	357162-7.6G
Vanadium	V	99.7% trace metals basis	thickness 0.25 mm	357170-15.2G
Iron	Fe	≥99.99% trace metals basis	thickness 0.25 mm	338141-1.2G 338141-5G
Iron	Fe	≥99.9% trace metals basis	thickness 0.1 mm	356808-2G 356808-8G
Cobalt	Co	≥99.99% trace metals basis	thickness 0.25 mm	266671-1.4G
Cobalt	Co	99.95% trace metals basis	thickness 0.1 mm	356867-2.2G 356867-8.8G
Nickel	Ni	99.98% trace metals basis	thickness 0.5 mm	357553-2.8G 357553-11.2G 357553-44.8G
Nickel	Ni	99.995% trace metals basis	thickness 0.25 mm	267007-1.4G 267007-5.6G
Nickel	Ni	99.98% trace metals basis	thickness 0.1 mm	357588-2.2G 357588-8.8G
Copper	Cu	99.999% trace metals basis	thickness 1.0 mm	266744-11G 266744-88G
Copper	Cu	99.98% trace metals basis	thickness 0.25 mm	349178-5.5G 349178-49.5G
Copper	Cu	99.98% trace metals basis	thickness 0.025 mm	349208-5G 349208-33G
Copper	Cu	99.98% trace metals basis	thickness 0.5 mm	349151-11G 349151-99G
Zinc	Zn	99.99% trace metals basis	thickness 1.0 mm	349410-4.5G 349410-18G
Zinc	Zn	99.999% trace metals basis	thickness 0.25 mm	267619-4.5G 267619-18G
Zirconium	Zr	99.98% trace metals basis	thickness 0.1 mm	419141-4.6G
Niobium	Nb	99.8% trace metals basis	thickness 0.25 mm	262781-32.1G
Molybdenum	Mo	≥99.9% trace metals basis	thickness 1.0 mm	357200-25.6G
Molybdenum	Mo	≥99.9% trace metals basis	thickness 0.1 mm	266922-10.2G
Molybdenum	Mo	≥99.9% trace metals basis	thickness 0.025 mm	357227-5.8G
Rhodium	Rh	99.9% trace metals basis	thickness 0.025 mm	357340-190MG
Palladium	Pd	99.9% trace metals basis	thickness 1.0 mm	348678-7.6G
Silver	Ag	99.9% trace metals basis	thickness 2.0 mm	326976-13.2G
Silver	Ag	99.99% trace metals basis	thickness 1.0 mm	369438-6.6G
Silver	Ag	99.9% trace metals basis	thickness 0.5 mm	345075-3.3G 345075-13.2G
Silver	Ag	99.9% trace metals basis	thickness 0.25 mm	326984-6.6G 326984-26.4G
Silver	Ag	99.9% trace metals basis	thickness 0.1 mm	265527-2.6G 265527-10.4G
Silver	Ag	99.9% trace metals basis	thickness 0.025 mm	265519-650MG 265519-2.6G 265519-13G

Name	Composition	Purity	Dimensions	Prod. No.
Cadmium	Cd	≥99.99% trace metals basis	thickness 0.5 mm	265411-11G
Indium	In	99.999% trace metals basis	thickness 0.5 mm	326631-2.3G 326631-36.8G
Indium	In	99.99% trace metals basis	thickness 0.25 mm	357294-4.6G 357294-18.4G 357294-41.4G
Indium	In	99.999% trace metals basis	thickness 0.1 mm	357308-1.8G 357308-7.2G
Tin	Sn	99.998% trace metals basis	thickness 0.5 mm	265756-9G 265756-36G
Tantalum	Ta	≥99.9% trace metals basis	thickness 0.25 mm	262897-10.4G 262897-41.6G
Tantalum	Ta	≥99.9% trace metals basis	thickness 0.05 mm	357243-8.4G 357243-18.9G
Tantalum	Ta	≥99.9% trace metals basis	thickness 0.025 mm	262919-9G 262919-31G
Tungsten	W	≥99.9% trace metals basis	thickness 0.5 mm	357189-24G 357189-96G
Tungsten	W	≥99.9% trace metals basis	thickness 0.25 mm	267546-12G 267546-48G
Tungsten	W	≥99.9% trace metals basis	thickness 0.127 mm	357197-6G 357197-24G
Tungsten	W	≥99.9% trace metals basis	thickness 0.05 mm	267538-2.4G
Rhenium	Re	99.98% trace metals basis	thickness 0.25 mm	267317-3.3G 267317-13.2G
Iridium	Ir	99.9% trace metals basis	thickness 0.25 mm	357324-3.5G
Platinum	Pt	99.99% trace metals basis	thickness 1.0 mm	349372-14G
Platinum	Pt	99.99% trace metals basis	thickness 0.5 mm	267260-7G 267260-14G
Platinum	Pt	99.99% trace metals basis	thickness 0.25 mm	349321-3.5G 349321-14G
Platinum	Pt	99.99% trace metals basis	thickness 0.1 mm	267252-1.3G 267252-5.3G 267252-5.6G
Platinum	Pt	99.99% trace metals basis	thickness 0.05 mm	349356-600MG 349356-2.4G
Platinum	Pt	99.99% trace metals basis	thickness 0.025 mm	349364-350MG 349364-1.4G
Gold	Au	99.99% trace metals basis	thickness 0.5 mm	265829-6G 265829-24G
Gold	Au	≥99.9% trace metals basis	thickness 0.25 mm	349240-3G 349240-12G
Gold	Au	99.99% trace metals basis	thickness 0.1 mm	265810-1.2G 265810-4.8G
Gold	Au	99.99% trace metals basis	thickness 0.05 mm	349275-600MG 349275-2.4G
Gold	Au	99.99% trace metals basis	thickness 0.025 mm	268461-300MG 268461-1.2G

Metal Slugs for Thermal Evaporation

For a complete list of available materials, visit Aldrich.com/metals

Name	Composition	Purity	Dimensions	Prod. No.
Aluminum	Al	99.999% trace metals basis	diam. × L 6.3 × 6.3 mm	433705-25G
Titanium	Ti	≥99.99% trace metals basis	diam. × L 6.3 × 6.3 mm	433667-4.8G
Titanium	Ti	≥99.99% trace metals basis	diam. × L 6.3 mm × 1.2 cm	433675-9.6G
Palladium	Pd	99.95% trace metals basis	diam. × L 0.9 × 1.2 cm	373192-10.9G
Palladium	Pd	99.95% trace metals basis	diam. × L 0.6 × 0.6 cm	373206-2.4G
Silver	Ag	99.99% trace metals basis	diam. × L 0.6 × 1.2 cm	373249-20.5G
Iridium	Ir	99.9% trace metals basis	diam. × L 0.6 × 1.2 cm	449229-7.6G
Platinum	Pt	99.99% trace metals basis	diam. × L 0.6 × 0.6 cm	373222-4.3G
Platinum	Pt	99.99% trace metals basis	diam. × L 0.3 × 0.6 cm	373230-1G
Gold	Au	99.99% trace metals basis	diam. × L 0.6 × 1.2 cm	373168-6.4G
Gold	Au	99.99% trace metals basis	diam. × L 0.6 × 0.6 cm	373176-3.9G
Gold	Au	99.99% trace metals basis	diam. × L 0.3 × 0.6 cm	373184-800MG 373184-3.2G

ALDRICH Materials Science

Pt/C Electrocatalysts

Accelerate Your Fuel Cell Research

Aldrich Materials Science offers a selection of new Pt-based catalysts for Proton Exchange Membrane Fuel Cells (PEMFC) and Direct Methanol Fuel Cells (DMFC). Benefits of these materials include:

- Consistent nanoparticle sizes for high surface areas and maximum electrocatalytic activity
- Increased stability and minimal particle growth at elevated temperatures
- Low-sulfur, highly conductive carbon supports to prevent catalyst poisoning

Advances in catalyst fabrication, such as the use of optimally sized platinum nanoparticles, enable increased performance of PEMFC and DMFC devices.[1] Alloys, such as Pt_3Co and Pt-Ru, also offer additional advantages due to their cost efficiency, high activity towards oxygen reduction, and enhanced tolerance to carbon monoxide.[2-3]

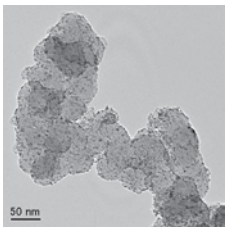

Pt/C, 20 wt.%
Prod. No. 738549

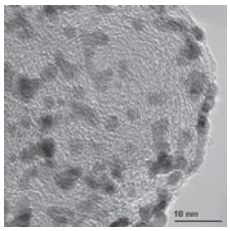

Pt_3Co/C, 30 wt.%
Prod. No. 738565

Catalyst	Name	Prod. No.
Pt/C	Platinum on graphitized carbon, 10 wt. % loading	738581
Pt/C	Platinum on graphitized carbon, 20 wt. % loading	738549
Pt/C	Platinum on graphitized carbon, 40 wt. % loading	738557
Pt_3Co/C	Platinum Cobalt on carbon, 30 wt. % Pt_3Co loading	738565
Pt-Ru/C	Platinum-Ruthenium alloy on graphitized carbon, 20 wt. % Pt, 10 wt. % Ru loading	738573

1. Starz, K.A.; Auer, A.; Lehmann, T.; Zuber, R. *J. Power Sources* **2000**, *86*, 237.
2. Steele, B.C.H.; Heinzel, A. *Nature* **2001**, *414*, 345.
3. Stamenkovic, V.; Schmidt, T.J.; Ross, P.N.; Markovic, N.M. *J. Phys. Chem. B* **2002**, *106*, 11970

For more information about fuel cell catalysts and membranes, visit our alternative energy portal at Aldrich.com/energy

Lanthanide Ions as Photon Managers for Solar Cells

Andries Meijerink
Condensed Matter and Interfaces, Debye Institute for NanoMaterials Science
Utrecht University, Princetonplein 5, 3584 CC Utrecht, The Netherlands
Email: a.meijerink@uu.nl

Introduction

Global energy consumption is on the rise and is projected to double by 2050, compared with worldwide energy consumption rates in 2001.[1] Sustainable energy production based on the direct conversion of energy radiated from the sun into heat or electricity is expected to gain importance, as it may be the only renewable source capable of generating sufficient energy to meet the long-term worldwide energy demand.[1,2] The capacity of photovoltaic cells to convert sunlight into electricity makes them prime candidates for effective large-scale capture and conversion of solar energy, but at present the contribution of photovoltaic energy is limited, due to its relatively high cost per kilowatt-hour. A reduction in price may be achieved by either lowering production costs or increasing conversion efficiency.

Crystalline Si (c-Si) solar cells dominate the photovoltaic market and have energy efficiencies around 15 %. In a solar cell, a single electron-hole pair is generated in a semiconductor upon absorbing a photon above the energy bandgap. The most significant loss mechanisms are due to relaxation of "hot" charge carriers that are created upon absorption of a high-energy photon and transmission of photons with energies below the bandgap of the semiconductor material.[3] The excess energy of high energy photons is rapidly lost as heat by thermalization. In a detailed balance model developed by Shockley and Queisser,[4] the theoretical efficiency limit for a single-junction solar cell with E_g equal to 1.1 eV can be determined to be 30%. A promising approach to raise the theoretical efficiency beyond the Shockley-Queisser limit is to adapt the solar spectrum through upconversion or downconversion. In upconversion, two low-energy photons are "added up" to give one higher-energy photon,[5] thus converting sub-bandgap photons, which are otherwise lost, into supra-bandgap photons, which can be absorbed. Downconversion, or "quantum cutting," is the opposite process, whereby one high-energy photon is "cut" into two lower-energy photons that are both absorbed. **Figure 1** shows the standard terrestrial solar spectrum and (in green) the fraction of the energy that can be harvested by a c-Si solar cell, assuming there are no other losses besides spectral mismatch losses.

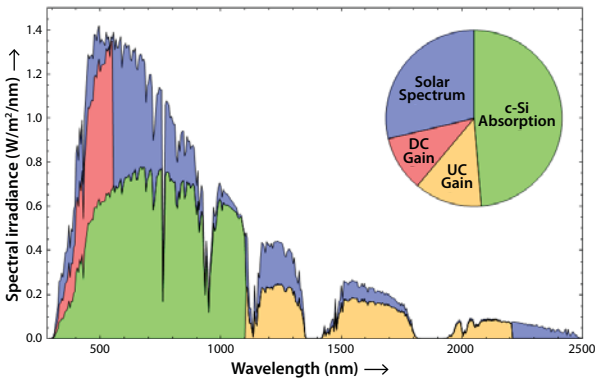

Figure 1. Potential efficiency gain of down- and 2-photon upconversion for a c-Si solar cell. The green part gives the part of the energy from the solar spectrum that can be converted into electrical energy by a c-Si solar cell, assuming no other losses than spectral mismatch losses. The yellow area gives the energy gain that can be obtained with an ideal upconverter, while the red part gives the maximum gain with an ideal downconverter.

The gain that can be achieved by using a perfect upconverter (in yellow) and perfect downconverter (in red) is about 20 % for each process for c-Si solar cells. In this review, the potential of using lanthanides as downconverters and upconverters will be outlined, after a brief introduction to the unique optical properties of lanthanides.

Luminescent Lanthanides

Lanthanides (Ln) are a group of elements that can be found at the bottom of the periodic table. The 4*f* inner shell of lanthanides is partially filled with electrons. They are mostly stable in the trivalent state, and the Ln^{3+} ions have the electronic configuration $4f^n5s^25p^6$, where *n* varies from 0 to 14. The partially filled 4*f* inner shell is responsible for the characteristic optical and magnetic properties of the lanthanides. The number of configurations for *n* electrons divided over the 14 4*f* orbitals is large (14/*n*), and all of the configurations can have different energies. In **Figure 2**, the energy level diagrams for the trivalent lanthanide ions, from Ce to Yb, are shown.

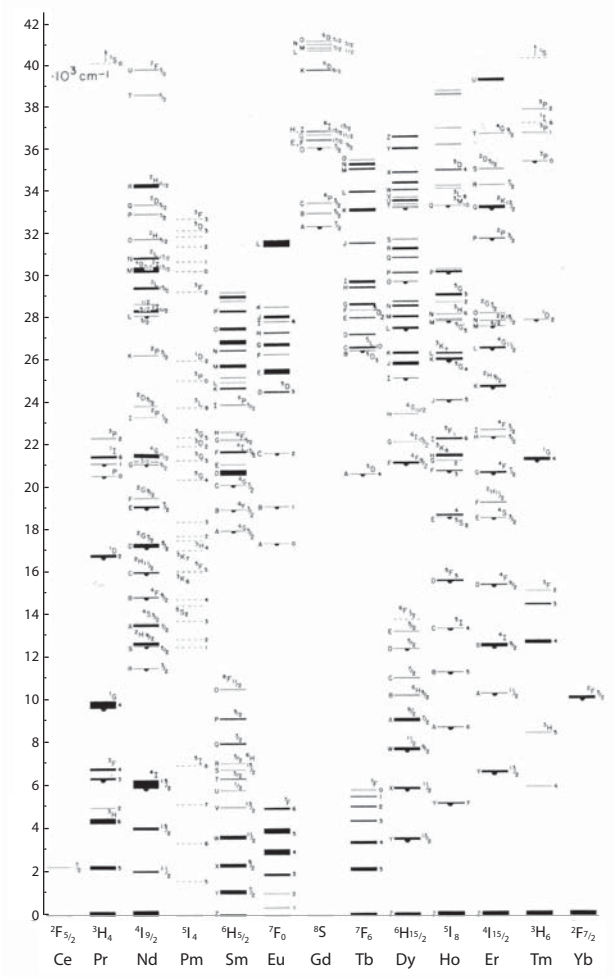

Figure 2. Free ion energy levels of the trivalent lanthanide ions from Ce^{3+} ($4f^1$) to Yb^{3+} ($4f^{13}$). Levels are labelled by term symbols or, for some higher levels, capital letters.

The horizontal black lines represent energy levels, labeled by term symbols $^{2S+1}L_J$. This diagram, often called the "Dieke diagram,"[6] exhibits the rich energy level structure of the free ions. It is also representative of the 4*f* energy level structure of these ions when doped into crystalline or glassy materials, because the optically-active 4*f* electrons are shielded from the host environment by the outer filled 5*s* and 5*p* orbitals. The shielding also results in sharp, atomic-like lines in the optical spectra. Quantum efficiency, defined as the number of photons emitted divided by the number of photons absorbed, can be very high, typically above 90%. The high efficiencies are the reason for the widespread application of lanthanides in light-emitting devices. In **Figure 3**, efficient luminescence is demonstrated for two applications.

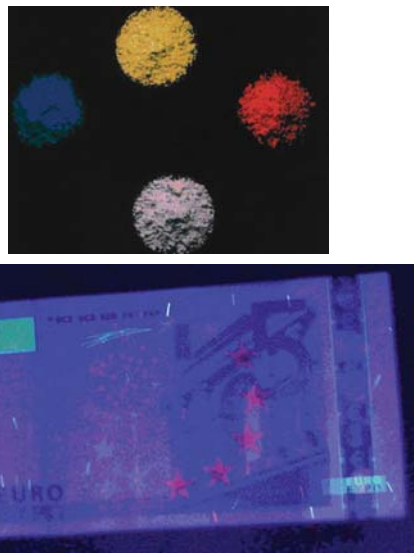

Figure 3. (top) Luminescence of blue (Eu^{2+}), green (Tb^{3+}) and red (Eu^{3+}) phosphors for (compact) fluorescent tubes under 254 nm UV irradiation. The white luminescence is obtained for a mixture of the blue, green and red phosphors. (bottom) Euro banknote under 360 nm UV irradiation. The red, green and blue luminescence from the stars and fibers is generated by Eu^{2+} (blue and green) and Eu^{3+} (red).

At the top, the emission of light by three lanthanide doped luminescent materials, or "phosphors," for application in fluorescent tubes is shown. At the bottom, the luminescence of a Euro banknote under UV-irradiation is shown as it is observed under the blacklight at a cash register. The red, green, and blue lights originate from Eu^{3+} and Eu^{2+} ions. The choice of safeguarding the *Euro* banknotes with the element *euro*pium has been deliberate.[7]

For up- and downconversion for solar cells, lanthanide ions are ideal candidates. The rich energy level structure allows many pathways to add or split the energy of incoming photons without significant energy losses. The process can take place within a single type of lanthanide ion, or it can involve energy transfer between two or more types of ions codoped within the same host material.

Upconversion

Upconversion with lanthanides was discovered in the early 1960s.[5] For the lanthanide ion couple Yb^{3+}-Er^{3+}, it was shown that upon infrared excitation of Yb^{3+} around 1000 nm, green and red luminescence from Er^{3+} is observed. The steps involved are illustrated in **Figure 4**.

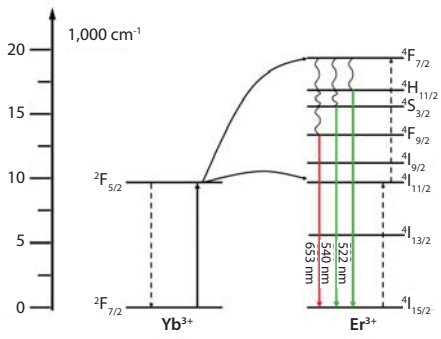

Figure 4. Schematic energy level scheme for the Yb/Er couple. The Yb^{3+} ion absorbs around 980 nm and transfers the energy from the $^2F_{5/2}$ level to the $^4I_{11/2}$ level of Er^{3+}. Subsequent energy transfer from a second excited Yb^{3+} ion to Er^{3+} ($^4I_{11/2}$), excites Er^{3+} ion to to the $^4F_{7/2}$ excited state. After multi-phonon relaxation to the lower lying $^4S_{3/2}$ and $^4F_{9/2}$ states, green and red emission are observed, as indicated.

The process was originally called "addition de photons par transfer d'energie" (APTE), but it is now generally known as energy transfer upconversion (ETU), and it is the most efficient mechanism for upconversion with lanthanide ions.[5] Different types of energy transfer mechanisms are possible, but non-radiative energy transfer via dipole-dipole interaction is mainly the dominant mechanism. Efficient energy transfer requires the ions to be in close proximity; thus, ETU requires high concentration of the dopants. One of the most efficient upconverter materials for NIR to VIS upconversion is $NaYF_4$: Er^{3+}, Yb^{3+}. Lanthanide upconverters have been applied in solar cells. Upconversion efficiency is low, and most demonstrations merely serve as proof of the principle showing that an increase in efficiency can be realized by applying an upconversion layer. In general, the upconverter is applied at the back of a cell as an electrically isolated layer. A back reflector reflects all emitted photons back into the solar cell. The first experiment was conducted on GaAs (Aldrich Prod. No. 329010) solar cells combined with a vitroceramic material doped with Yb^{3+} and Er^{3+} under extremely high excitation densities. An efficiency of 2.5 % of the solar cell was obtained. In 2005, Shalav *et al.*[8] showed upconversion under lower excitation density of 2.4 W/cm^2 reaching 3.4 % quantum efficiency at 1,523 nm in a crystalline silicon solar cell with $NaYF_4$ doped with Er^{3+} as upconverter. Since c-Si has a rather small bandgap (1.12 eV), transmission losses are not as high as for wider bandgap solar cells. Therefore, the efficiency gain for larger bandgap solar cells can be higher.

Presently, upconversion efficiencies are still rather low; only at high excitation densities, exceeding the solar power density, are efficiencies above 1 % reached. Concentration of solar light is needed. In addition, it is crucial to broaden the absorption spectrum, as the absorption lines for lanthanide upconverters are narrow, and absorption strengths are low for the parity forbidden transitions within the $4f^n$ configuration. Broadening of the absorption spectrum for lanthanide upconverters can be achieved by using a sensitizer with a broad absorption band and a narrow emission line resonant with the lanthanide absorption line. Sensitization can be achieved by an external sensitizer (e.g., quantum dots), or an internal sensitizer (e.g., transition metal ions). Even more challenging are options to enhance upconversion efficiencies by manipulating emission and excitation processes through plasmonic coupling.[9] The use of plasmonic effects with upconverter materials is a new and emerging field, with many possibilities and challenges.

Downconversion

The idea to obtain quantum efficiencies above 100 % by creating multiple photons through "cutting" a single photon into two lower-energy photons was first proposed by Dexter in 1957.[10] The mechanism involved the simultaneous energy transfer from a donor to two acceptors, each accepting half the energy of the excited donor. It was not until 1974 that experimental evidence for quantum yields above 100 % was obtained, for YF_3:Pr^{3+}.[11,12] The mechanism was not the one proposed by Dexter, but it involved two sequential emission steps from the high-energy $^1S_0$. Later, quantum cutting via two sequential energy transfer steps in the Gd^{3+}-Eu^{3+} couple was discovered and, based on the analogy of the two-step energy transfer process in upconversion, it was called "downconversion."[13] The aim in all this work was to achieve the emission of two visible photons from a single UV photon in order to boost the efficiency of light-emitting devices. The potential of down-conversion for increasing the efficiency of solar cells was realized soon afterwards.[2] The first experimental demonstration of downconversion for solar cells involved the Tb^{3+}-Yb^{3+} couple, where quantum cutting was achieved through cooperative energy transfer from Tb^{3+} to two Yb^{3+} ions, the very mechanism suggested almost 50 years earlier by Dexter.[15] It is evident from the Dieke diagram (**Figure 2**) that the energy level structure of Yb^{3+} is ideally suited for use in downconversion for c-Si solar cells. The Yb^{3+} ion has a single excited state approximately 10,000 cm^{-1} above the ground state, corresponding to an emission of around 1,000 nm. The absence of other energy levels allows Yb^{3+} to exclusively "pick up" energy packages of 10,000 cm^{-1} from other codoped lanthanide ions and emit photons at ~1,000 nm, which can be absorbed by c-Si. Efficient downconversion using Yb^{3+} via resonant energy transfer requires donor ions with an energy level at about 20,000 cm^{-1} and an intermediate energy level at approximately 10,000 cm^{-1}. Examination of **Figure 2** reveals potential ion couples, such as Er^{3+} - Yb^{3+}, Nd^{3+} - Yb^{3+}, Ho^{3+} - Yb^{3+}, and Pr^{3+} - Yb^{3+}. As an example, **Figure 5** shows the energy transfer processes leading downconversion for the Pr^{3+}-Yb^{3+} couple.

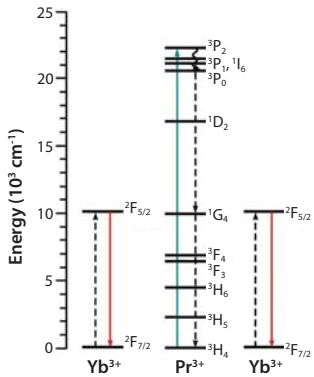

Figure 5. Energy levels and quantum cutting mechanism for the Pr^{3+} - Yb^{3+} couple. A two-step energy transfer occurs upon excitation into the ^3P_J (J=0, 1, 2) and $^1I_6$ levels of Pr^{3+}. A single visible photon absorbed by these levels is thereby converted into two ~1,000 nm photons. Solid, dotted, and curved arrows represent optical transitions, nonradiative energy transfer processes, and nonradiative relaxation, respectively.

After excitation into one of the ^3P_J levels between 450 and 490 nm, efficient two-step energy transfer to two neighboring Yb^{3+} ions occurs with internal quantum efficiencies close to 200 %. Both Yb^{3+} ions can emit a 1,000 nm photon that can be absorbed by a c-Si solar cell.

The promising results of downconversion with lanthanides does not mean that one can expect implementation of downconversion materials in solar cells in the near future. On the contrary, serious challenges need to be addressed before downconversion materials can be applied. A major limitation, just as for upconversion, is the weak absorption for $4f^n$ transitions. A solution may be a sensitizer that absorbs efficiently in the UV/VIS and transfers the energy to the downconversion couple. Work on the sensitization is only just starting. A second issue is concentration quenching. High Yb^{3+}-concentrations are needed to achieve complete energy transfer to the Yb^{3+} acceptor ions. At these high concentrations, quenching of the emission occurs through energy migration over the Yb^{3+}-sublattice (concentration quenching) and lowers efficiency. Finally, if an efficient downconversion couple is developed, the material needs to be incorporated in a transparent layer on top of the solar cell. To prevent losses due to isotropic emission, an anti-reflective coating for the 1,000-nm Yb^{3+} emission is required on top of the downconversion layer. Clearly, the road toward implementation is long.

Conclusions

Spectral conversion for solar cells is an emerging concept in the field of photovoltaics, and it has the potential to increase significantly the efficiency of solar cells. Lanthanide ions are ideal candidates for spectral conversion, due to their high luminescence efficiencies and rich energy level structure that allows for great flexibility in the upconversion and downconversion of photons in a wide spectral region (NIR-VIS-UV). Proof-of-concept experiments have been reported for upconversion, demonstrating an increase in efficiency for sub-bandgap illumination for different types of solar cells by application of upconverter materials. The challenges lie in improving upconversion efficiency, especially for the relatively low excitation densities that are typical for solar illumination.

Quantum cutting through downconversion has only been studied in the last decade. It offers great potential for efficiency enhancement for narrow bandgap solar cells, such as c-Si solar cells. Efficient down-conversion has been reported for several lanthanide couples. In these couples, Yb^{3+} serves as an ideal acceptor with a single excited state, just above the bandgap of c-Si. High internal quantum yields (close to 200 %) have been demonstrated and are independent of the incident power. Before implementation in solar cell systems can be realized, some serious issues need to be addressed: sensitization, concentration quenching, and a transparent downconversion layer on top of the solar cell. Research on solving the various issues is in progress, and new results can be expected in the coming years. Based on these results, it will become clear if photon management using lanthanides is indeed a viable option to realize more efficient solar cells.

References

(1) Lewis, N. S.; Nocera, D. G. *PNAS* **2006**, *103*, 15729.
(2) Morton, O. *Nature* **2006**, *443*, 19.
(3) Richards, B. S. *Sol. Energy Mater. Sol. Cells* **2006**, *90*, 2329.
(4) Shockley, W.; Queisser, H. J. *J. Appl. Phys.* **1961**, *32*, 510.
(5) Auzel, F. *Chem. Rev.* **2004**, *104*, 139.
(6) Dieke, G. H.; Crosswhite, H. M. *Applied Optics* **1963**, *2*, 675.
(7) Suyver, F.; Meijerink, A. *Chemisch2Weekblad* **2002**, *4*, 12.
(8) Shalav, A.; Richards, B. S.; Trupke, T.; Kramer, K. W.; Gudel, H. U. *Appl. Phys. Lett.* **2005**, *86*, 013505.
(9) Baluschev, S.; Yu, F.; Miteva, T.; Ahl, S.; Yasuda, A.; Nelles, G.; Knoll, W.; Wegner, G. *Nano Lett.* **2005**, *12*, 2482.
(10) Dexter, D. L. *Phys. Rev.* **1957**, *108*, 630.
(11) Sommerdijk, J. L.; Bril, A.; de Jager, A. W. *J. Lumin.* **1974**, *8*, 341.
(12) Piper, W. W.; DeLuca, J. A.; Ham, F. S. *J. Lumin.* **1974**, *8*, 344.
(13) Wegh, R. T.; Donker, H.; Oskam, K. D.; Meijerink, A. *Science* **1999**, *283*, 663.
(14) Trupke, T.; Green, M. A.; Würfel, P. *J. Appl. Phys.* **2002**, *92*, 1668.
(15) Vergeer, P.; Vlugt, T. J. H.; Kox, M. H. F.; den Hertog, M. I.; van der Eerden, J. P. J. M.; Meijerink, A. *Phys. Rev. B* **2005**, *71*, 014119.
(16) van der Ende, B. M.; Aarts, L.; Meijerink, A. *Phys. Chem. Chem. Phys.* **2009**, *11*, 11081.

Phosphor Host Materials

For a complete list of available materials, visit Aldrich.com/renewable

Name	Composition	Purity	Form	Prod. No.
Sodium fluoride	NaF	99.99% trace metals basis	powder	450022-5G 450022-25G
Sodium fluoride	NaF	99.99% trace metals basis	powder	215309-10G 215309-50G 215309-250G
Magnesium oxide	MgO	99.995% trace metals basis	powder	529699-10G 529699-50G
Magnesium oxide	MgO	99.99% trace metals basis	powder	203718-5G 203718-25G 203718-100G
Aluminum acetylacetonate	$Al(C_5H_7O_2)_3$	99.999%	powder	674753-5G 674753-25G
Aluminum *tert*-butoxide	$Al[OC(CH_3)_3]_3$	-	powder	235849-10G 235849-50G
Aluminum ethoxide	$Al(OC_2H_5)_3$	97%	powder and chunks	235857-5G 235857-25G 235857-100G
Aluminum isopropoxide	$Al[OCH(CH_3)_2]_3$	≥99.99% trace metals basis	powder and chunks	229407-10G 229407-50G 229407-250G
Aluminum hydroxide hydrate	$Al(OH)_3 \cdot xH_2O$	-	powder	A1577-500G A1577-1KG
Silicon aluminum oxynitride	$SiAl_6N_6O_2$	-	-	752614-25G
Calcium nitride	Ca_3N_2	95%	powder	415103-25G 415103-100G
Calcium sulfide	CaS	≥99.9% trace metals basis	powder	409553-10G 409553-50G
Calcium fluoride	CaF_2	99.99% trace metals basis	random crystals	378801-25G
Calcium fluoride	CaF_2	99.99% trace metals basis	powder	449717-5G 449717-25G
Gallium nitride	GaN	99.99% trace metals basis	powder	481769-10G 481769-50G
Strontium	Sr	99%	random pieces	343730-10G 343730-50G
Strontium fluoride	SrF_2	99.995% trace metals basis	solid	652466-25G 652466-100G
Strontium fluoride	SrF_2	99.99% trace metals basis	powder	450030-10G 450030-50G
Yttrium(III) oxide	Y_2O_3	99.999% trace metals basis	powder	204927-10G 204927-50G
Yttrium(III) oxide	Y_2O_3	99.99% trace metals basis	powder	205168-10G 205168-50G 205168-250G
Yttrium(III) fluoride	YF_3	99.99% trace metals basis	powder	451371-10G
Yttrium(III) chloride	YCl_3	99.99% trace metals basis	beads	751960-5G
Yttrium(III) tris(isopropoxide)	$YC_9H_{21}O_3$	-	solid	665916-500MG
Yttrium aluminum oxide	$Y_3Al_5O_{12}$	99% trace metals basis	nanopowder	634638-25G
Barium carbonate	$BaCO_3$	99.999% trace metals basis	powder and chunks	202711-25G 202711-100G
Barium fluoride	BaF_2	98%	powder	236101-500G

Name	Composition	Purity	Form	Prod. No.
Lanthanum(III) nitrate hexahydrate	$La(NO_3)_3 \cdot 6H_2O$	99.999% trace metals basis	solid	203548-25G 203548-100G 203548-500G
Lanthanum(III) nitrate hexahydrate	$La(NO_3)_3 \cdot 6H_2O$	99.99% trace metals basis	solid	331937-5G 331937-100G 331937-500G
Lanthanum(III) phosphate hydrate	$LaPO_4 \cdot xH_2O$	≥99.99% trace metals basis	chunks	587176-25G

Phosphor Activator Materials

For a complete list of available materials, visit Aldrich.com/renewable

Name	Composition	Purity	Form	Prod. No.
Cerium(IV) oxide	CeO_2	99.9% trace metals basis	fused pieces	342955-50G
Cerium(IV) oxide	CeO_2	99.995% trace metals basis	powder	202975-10G 202975-50G
Cerium(III) bromide heptahydrate	$CeBr_3 \cdot 7H_2O$	99.99% trace metals basis	-	737844-5G
Cerium(III) nitrate hexahydrate	$Ce(NO_3)_3 \cdot 6H_2O$	99.999% trace metals basis	crystals and lumps	202991-25G 202991-125G
Europium(II) bromide	$EuBr_2$	99.99% trace metals basis	-	751936-1G
Europium(II) iodide	EuI_2	99.999%	beads	751499-5G
Europium(III) nitrate hydrate	$Eu(NO_3)_3 \cdot xH_2O$	99.99% trace metals basis	solid	254061-1G 254061-10G
Europium(III) nitrate pentahydrate	$Eu(NO_3)_3 \cdot 5H_2O$	99.9% trace metals basis	crystals and lumps	207918-1G 207918-10G 207918-50G
Europium(III) oxide	Eu_2O_3	99.999% trace metals basis	powder and chunks	323543-1G 323543-5G
Europium(III) oxide	Eu_2O_3	99.99% trace metals basis	powder	203262-5G 203262-25G
Gadolinium(III) chloride	$GdCl_3$	99.99% trace metals basis	beads	735949-5G
Gadolinium(III) nitrate hexahydrate	$Gd(NO_3)_3 \cdot 6H_2O$	99.999% trace metals basis	crystals and lumps	217190-10G
Gadolinium(III) nitrate hexahydrate	$Gd(NO_3)_3 \cdot 6H_2O$	99.99% trace metals basis	solid	451134-10G 451134-50G
Terbium(III) nitrate hexahydrate	$Tb(NO_3)_3 \cdot 6H_2O$	99.999% trace metals basis	crystals and lumps	217212-2G 217212-10G
Terbium(III) nitrate pentahydrate	$Tb(NO_3)_3 \cdot 5H_2O$	99.9% trace metals basis	solid	325945-5G 325945-25G
Terbium(III) oxide	Tb_2O_3	99.99% trace metals basis	powder	590509-2G 590509-10G
Terbium(III,IV) oxide	Tb_4O_7	99.999% trace metals basis	powder	204579-2G
Thulium(III) nitrate pentahydrate	$Tm(NO_3)_3 \cdot 5H_2O$	99.9%	powder	325996-1G 325996-5G
Ytterbium(III) nitrate pentahydrate	$Yb(NO_3)_3 \cdot 5H_2O$	99.999%	chunks	217220-5G 217220-25G
Ytterbium(III) nitrate pentahydrate	$Yb(NO_3)_3 \cdot 5H_2O$	99.9% trace metals basis	crystals and lumps	209147-10G 209147-50G

Materials for Inorganic Photovoltaics

For a complete list of available materials, visit Aldrich.com/renewable

Name	Composition	Purity	Form	Prod. No.
Sulfur	S	99.998% trace metals basis	powder or flakes	213292-10G 213292-50G 213292-250G
Sulfur	S	≥99.99% trace metals basis	flakes	344621-50G 344621-250G
Copper	Cu	99.9999% trace metals basis	rod, diam. 11 mm	365327-21.5G 365327-172G
Copper	Cu	99.9998% trace metals basis	rod, diam. 19 mm	264857-56G
Copper	Cu	99.9995% trace metals basis	beads	254177-25G 254177-125G
Copper	Cu	99.999% trace metals basis	platelets, thickness 6.3 mm	518905-26G
Copper	Cu	99.999% trace metals basis	powder	203122-10G 203122-50G
Copper(II) chloride	$CuCl_2$	≥99.995% trace metals basis	powder	451665-5G 451665-25G
Copper(I) chloride	CuCl	≥99.99% trace metals basis	beads	651745-5G 651745-25G
Copper(I) chloride	CuCl	≥99.995% trace metals basis	powder	229628-10G 229628-100G

Name	Composition	Purity	Form	Prod. No.
Copper(II) chloride	$CuCl_2$	99.999% trace metals basis	powder	203149-10G 203149-50G
Copper(II) acetate	$Cu(CO_2CH_3)_2$	99.999% trace metals basis	powder	517453-5G 517453-25G
Gallium	Ga	99.9995% trace metals basis	-	203319-1G 203319-5G 203319-25G
Gallium	Ga	99.999% trace metals basis	-	263273-10G 263273-50G
Gallium(II) chloride	Ga_2Cl_4	99.999% trace metals basis	crystalline	413089-1G 413089-5G
Gallium(III) chloride	$GaCl_3$	≥99.999% trace metals basis	beads	427128-5G 427128-25G 427128-100G
Gallium(III) chloride	$GaCl_3$	99.99% trace metals basis	beads	450898-5G 450898-25G 450898-50G
Gallium arsenide	GaAs	99.999% trace metals basis	pieces	329010-1G
Selenium	Se	≥99.99% trace metals basis	pellets	209643-50G 209643-250G
Selenium	Se	≥99.999% trace metals basis	pellets	204307-5G 204307-20G 204307-100G
Selenium	Se	99.99% trace metals basis	powder	229865-5G 229865-20G 229865-100G
Indium	In	99.999% trace metals basis	beads, diam. 2-5 mm	264113-5G 264113-25G
Indium(III) oxide	In_2O_3	99.999% trace metals basis	powder	203424-5G 203424-25G
Indium(III) oxide	In_2O_3	99.99% trace metals basis	powder	289418-10G 289418-50G
Indium(I) chloride	InCl	99.999%	powder	449210-2G 449210-10G
Indium(II) chloride	$InCl_2$	99.9%	powder	548456-1G 548456-10G
Indium(III) chloride	$InCl_3$	≥99.999% trace metals basis	powder	429414-5G 429414-25G
Indium(III) chloride	$InCl_3$	99.999% trace metals basis	powder and chunks	203440-1G 203440-10G 203440-50G
Indium(III) selenide	In_2Se_3	-	lumps	403318-5G
Indium antimonide	InSb	-	-	740942-5G

Quantum Dots

For a complete list of available materials, visit Aldrich.com/quantumdots

Name	Particle Size (nm), λ_{abs} (nm)	Fluorescence Emission (nm)	Prod. No.
Lumidot™ CdS, 380, core-type quantum dots, 5 mg/mL in toluene,380 core-type quantum dots	~2.3, 350-370	λ_{em} = 370-390	662429-10ML
Lumidot™ CdS, 400, core-type quantum dots, 5 mg/mL in toluene, 400 core-type quantum dots	~2.9, 370-390	λ_{em} = 390-410	662410-10ML
Lumidot™ CdS, 420, core-type quantum dots, 5 mg/mL in toluene, 420 core-type quantum dots	~3.4, 390-410	λ_{em} = 410-430	662402-10ML
Lumidot™ CdS, 440, core-type quantum dots, 5 mg/mL in toluene, 440 core-type quantum dots	~4.2, 410-430	λ_{em} = 430-450	662380-10ML
Lumidot™ CdS, 460, core-type quantum dots, 5 mg/mL in toluene, 460 core-type quantum dots	~5.0, 430-450	λ_{em} = 450-470	662372-10ML
Lumidot™ CdS, 480, core-type quantum dots, 5 mg/mL in toluene, 480 core-type quantum dots	~5.6, 450-470	λ_{em} = 470-490	662364-10ML
Lumidot™ CdSe, 480, core-type quantum dots, 5 mg/mL in toluene, 480 core-type quantum dots	~2.1, 455-465	λ_{em} = 475-485	662356-10ML
Lumidot™ CdSe, 520, core-type quantum dots, 5 mg/mL in toluene, 520 core-type quantum dots	~2.5, 495-505	λ_{em} = 515-525	662437-10ML
Lumidot™ CdSe, 560, core-type quantum dots, 5 mg/mL in toluene, 560 core-type quantum dots	~3.3, 535-545	λ_{em} = 555-565	662445-10ML
Lumidot™ CdSe, 590, core-type quantum dots, 5 mg/mL in toluene, 590 core-type quantum dots	4.0-4.3, 565-575	λ_{em} = 585-595	662607-10ML
Lumidot™ CdSe, 610, core-type quantum dots, 5 mg/mL in toluene, 610 core-type quantum dots	~5.0, 585-595	λ_{em} = 605-615	662488-10ML
Lumidot™ CdSe, 640, core-type quantum dots, 5 mg/mL in toluene, 640 core-type quantum dots	~6.6, 615-625	λ_{em} = 635-645	662461-10ML

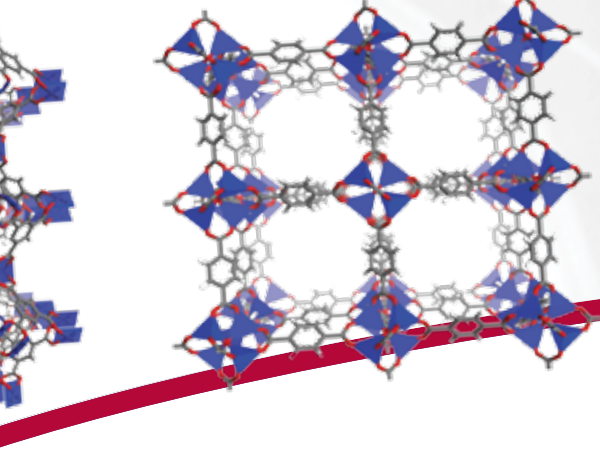

ALDRICH Materials Science

Aldrich® MOF Constructor

An Easy Way to Design Your Own MOF

Metal-Organic Frameworks (MOFs) are porous coordination networks with record-setting surface areas. MOFs are built from metal ion clusters connected by organic linker molecules and are designed for applications requiring high surface areas.

Aldrich Materials Science offers a *broad variety* of high-purity metal cluster secondary building units (SBUs), metal salts, organic linkers and solvents, as well as Basolite® MOFs or, request *custom-designed materials* for your MOF research.

High-purity Metal Cluster SBUs for Metal-Organic Frameworks

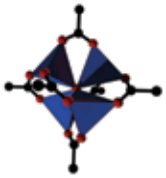

Tetrameric
Zn cluster
Prod. No. 741051

Trimeric
Fe cluster
Prod. No. 749141

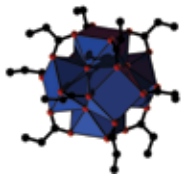

Hexameric
Zr cluster
Prod. No. 749168

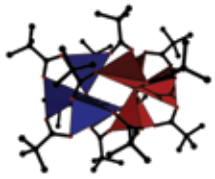

Tetrameric
Co cluster
Prod. No. 749125

Organic Linker Molecules for Metal-Organic Frameworks

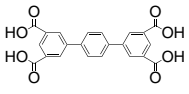

H4TPTC
Prod. No. 716502

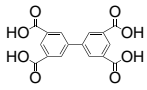

H4BPTC
Prod. No. 720968

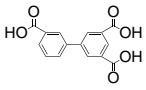

H3BHTC
Prod. No. 714747

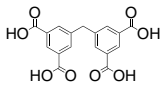

H4MDIP
Prod. No. 731706

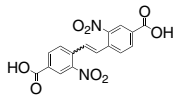

H2DNSDC
Prod. No. 721239

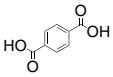

TPA, H2BDC
Prod. No. 185361

H2BDC-OH
Prod. No. 752525

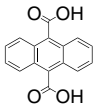

H2ADC
Prod. No. 724440

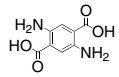

H2DATA
Prod. No. 717312

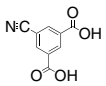

H2CyIPT
Prod. No. 714739

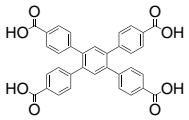

H4TCPB
Prod. No. 715298

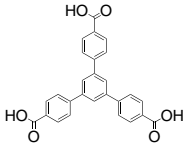

H3BTB
Prod. No. 686859

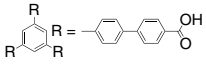

H3TCBPB
Prod. No. 706884

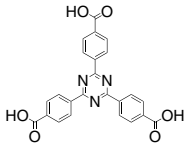

H3TATB
Prod. No. 744175

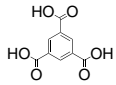

TMA, H3BTC
Prod. No. 482749

Contact us at **matsci@sial.com** to discuss materials for your own MOF.

For more information, visit **Aldrich.com/renewable**

Sigma-Aldrich
3050 Spruce Street
St. Louis, MO 63103 USA

Sigma-Aldrich® Worldwide Offices

Argentina
Free Tel: 0810 888 7446
Tel: (+54) 11 4556 1472
Fax: (+54) 11 4552 1698

Australia
Free Tel: 1800 800 097
Free Fax: 1800 800 096
Tel: (+61) 2 9841 0555
Fax: (+61) 2 9841 0500

Austria
Tel: (+43) 1 605 81 10
Fax: (+43) 1 605 81 20

Belgium
Tel: (+32) 3 899 13 01
Fax: (+32) 3 899 13 11

Brazil
Free Tel: 0800 701 7425
Tel: (+55) 11 3732 3100
Fax: (+55) 11 5522 9895

Canada
Free Tel: 1800 565 1400
Free Fax: 1800 265 3858
Tel: (+1) 905 829 9500
Fax: (+1) 905 829 9292

Chile
Tel: (+56) 2 495 7395
Fax: (+56) 2 495 7396

People's Republic of China
Free Tel: 800 819 3336
Tel: (+86) 21 6141 5566
Fax: (+86) 21 6141 5567

Czech Republic
Tel: (+420) 246 003 200
Fax: (+420) 246 003 291

Denmark
Tel: (+45) 43 56 59 00
Fax: (+45) 43 56 59 05

Finland
Tel: (+358) 9 350 9250
Fax: (+358) 9 350 92555

France
Free Tel: 0800 211 408
Free Fax: 0800 031 052
Tel: (+33) 474 82 28 88
Fax: (+33) 474 95 68 08

Germany
Free Tel: 0800 51 55 000
Free Fax: 0800 64 90 000
Tel: (+49) 89 6513 0
Fax: (+49) 89 6513 1169

Hungary
Tel: (+36) 1 235 9055
Fax: (+36) 1 235 9068

India
Telephone
Bangalore: (+91) 80 6621 9400
New Delhi: (+91) 11 4358 8000
Mumbai: (+91) 22 4087 2364
Pune: (+91) 20 4146 4700
Hyderabad: (+91) 40 3067 7450
Kolkata: (+91) 33 4013 8000
Fax
Bangalore: (+91) 80 6621 9550
New Delhi: (+91) 11 4358 8001
Mumbai: (+91) 22 2579 7589
Pune: (+91) 20 4146 4777
Hyderabad: (+91) 40 3067 7451
Kolkata: (+91) 33 4013 8016

Ireland
Free Tel: 1800 200 888
Free Fax: 1800 600 222
Tel: +353 (0) 402 20370
Fax: + 353 (0) 402 20375

Israel
Free Tel: 1 800 70 2222
Tel: (+972) 8 948 4222
Fax: (+972) 8 948 4200

Italy
Free Tel: 800 827 018
Tel: (+39) 02 3341 7310
Fax: (+39) 02 3801 0737

Japan
Tel: (+81) 3 5796 7300
Fax: (+81) 3 5796 7315

Korea
Free Tel: (+82) 80 023 7111
Free Fax: (+82) 80 023 8111
Tel: (+82) 31 329 9000
Fax: (+82) 31 329 9090

Luxembourg
Tel: (+32) 3 899 1301
Fax: (+32) 3 899 1311

Malaysia
Tel: (+60) 3 5635 3321
Fax: (+60) 3 5635 4116

Mexico
Free Tel: 01 800 007 5300
Free Fax: 01 800 712 9920
Tel: (+52) 722 276 1600
Fax: (+52) 722 276 1601

The Netherlands
Tel: (+31) 78 620 5411
Fax: (+31) 78 620 5421

New Zealand
Free Tel: 0800 936 666
Free Fax: 0800 937 777
Tel: (+61) 2 9841 0555
Fax: (+61) 2 9841 0500

Norway
Tel: (+47) 23 17 60 00
Fax: (+47) 23 17 60 10

Poland
Tel: (+48) 61 829 01 00
Fax: (+48) 61 829 01 20

Portugal
Free Tel: 800 202 180
Free Fax: 800 202 178
Tel: (+351) 21 924 2555
Fax: (+351) 21 924 2610

Russia
Tel: (+7) 495 621 5828
Fax: (+7) 495 621 6037

Singapore
Tel: (+65) 6779 1200
Fax: (+65) 6779 1822

Slovakia
Tel: (+421) 255 571 562
Fax: (+421) 255 571 564

South Africa
Free Tel: 0800 1100 75
Free Fax: 0800 1100 79
Tel: (+27) 11 979 1188
Fax: (+27) 11 979 1119

Spain
Free Tel: 900 101 376
Free Fax: 900 102 028
Tel: (+34) 91 661 99 77
Fax: (+34) 91 661 96 42

Sweden
Tel: (+46) 8 742 4200
Fax: (+46) 8 742 4243

Switzerland
Free Tel: 0800 80 00 80
Free Fax: 0800 80 00 81
Tel: (+41) 81 755 2511
Fax: (+41) 81 756 5449

Thailand
Tel: (+66) 2 126 8141
Fax: (+66) 2 126 8080

United Kingdom
Free Tel: 0800 717 181
Free Fax: 0800 378 785
Tel: (+44) 1747 833 000
Fax: (+44) 1747 833 313

United States
Toll-Free: 800 325 3010
Toll-Free Fax: 800 325 5052
Tel: (+1) 314 771 5765
Fax: (+1) 314 771 5757

Vietnam
Tel: (+84) 8 3516 2810
Fax: (+84) 8 6258 4238

Internet
sigma-aldrich.com

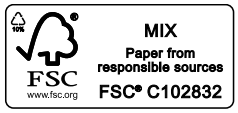

Enabling Science to Improve the Quality of Life

Order/Customer Service (800) 325-3010 • Fax (800) 325-5052
Technical Service (800) 325-5832 • sigma-aldrich.com/techservice
Development/Custom Manufacturing Inquiries SAFC® (800) 244-1173
Safety-related Information sigma-aldrich.com/safetycenter

World Headquarters
3050 Spruce St.
St. Louis, MO 63103
(314) 771-5765
sigma-aldrich.com

OAI
77358-512840
1111